Article

Neuron

Reliable Sequential Activation of Neural Assemblies by Single Pyramidal Cells in a Three-Layered Cortex

Highlights

- The consequences of activating single pyramidal cells were studied in turtle cortex
- Two spikes from single neurons activated tens of neurons sequentially and reliably
- The activated neurons were both interneurons and other pyramidal cells
- The evoked sequences lasted up to 200 ms, spread over 1 mm^2, and never ignited cortex

Authors

Mike Hemberger, Mark Shein-Idelson, Lorenz Pammer, Gilles Laurent

Correspondence

gilles.laurent@brain.mpg.de

In Brief

Hemberger et al. examine the actions of single neurons on surrounding networks in reptilian cortex. Cortical pyramidal neurons can initiate neuronal sequences reminiscent of hypothesized "synfire chains," suggesting the existence of a landscape of preferred paths for cortical information flow.

Hemberger et al., 2019, Neuron *104*, 353–369
October 23, 2019
https://doi.org/10.1016/j.neuron.2019.07.017

CellPress

Neuron
Article

CellPress

Reliable Sequential Activation of Neural Assemblies by Single Pyramidal Cells in a Three-Layered Cortex

Mike Hemberger,[1] Mark Shein-Idelson,[1,2] Lorenz Pammer,[1] and Gilles Laurent[1,3,*]
[1]Max Planck Institute for Brain Research, Frankfurt am Main, 60438 Germany
[2]Department of Neurobiology, George S. Wise Faculty of Life Sciences, Sagol School for Neuroscience, Tel-Aviv University, Tel Aviv, Israel
[3]Lead Contact
*Correspondence: gilles.laurent@brain.mpg.de
https://doi.org/10.1016/j.neuron.2019.07.017

SUMMARY

Recent studies reveal the occasional impact of single neurons on surround firing statistics and even simple behaviors. Exploiting the advantages of a simple cortex, we examined the influence of single pyramidal neurons on surrounding cortical circuits. Brief activation of single neurons triggered reliable sequences of firing in tens of other excitatory and inhibitory cortical neurons, reflecting cascading activity through local networks, as indicated by delayed yet precisely timed polysynaptic subthreshold potentials. The evoked patterns were specific to the pyramidal cell of origin, extended over hundreds of micrometers from their source, and unfolded over up to 200 ms. Simultaneous activation of pyramidal cell pairs indicated balanced control of population activity, preventing paroxysmal amplification. Single cortical pyramidal neurons can thus trigger reliable postsynaptic activity that can propagate in a reliable fashion through cortex, generating rapidly evolving and non-random firing sequences reminiscent of those observed in mammalian hippocampus during "replay" and in avian song circuits.

INTRODUCTION

The cerebral cortex is an ancient pallial structure that evolved in ancestral amniotes some 320 million years ago (Puelles et al., 2017; Tosches et al., 2018), before the split between the sauropsids ("reptilian" lineage, including birds and non-avian reptiles) and the synapsids, the amniote ancestors of mammals. Ancestral cortex had three layers, as do the cortices of extant non-avian reptiles and the hippocampus and piriform cortex of mammals (Striedter, 1997). In birds, a reorganization of the pallium led to a loss of the ancestral layered architecture of cortex (Jarvis et al., 2005), and the precise matching of avian pallial to non-avian cortical territories is not entirely resolved. In the mammalian lineage, an ancestral anterior dorsal cortex located between hippocampus and piriform cortex, evolved into the six-layered neocortex (Montiel et al., 2016; Naumann et al., 2015; Tosches et al., 2018). The cortices of today's living reptiles and mammals thus all originate from a common primordial cortex, suggesting that they may retain traces of this common ancestry in their structure, connectivity, and function.

Trusting that the identification of functional principles benefit from the study of many appropriately chosen model systems (Fournier et al., 2015; Hemberger et al., 2016), we examine circuit dynamics in the reptilian brain, exploiting its evolutionary links to that of other amniotes, its simplicity, and its resistance to hypoxia (Connors and Kriegstein, 1986; Kriegstein and Connors, 1986). We took advantage of the three-layered reptilian cortex to sample action potentials from hundreds of neurons at once in intact cortical explants (Shein-Idelson et al., 2017). Excitatory glutamatergic pyramidal neurons (PNs) are packed in the only cellular layer (L2). Layers L1 and L3 contain GABAergic interneurons and neuropil. While examining intra-cortical connectivity, an observation led us to explore the effects of minimal activation of single pyramidal cells. This approach has been used before in mammals (Brecht et al., 2004; Houweling and Brecht, 2008; Li et al., 2009; London et al., 2010) and established that minimal manipulation of single cortical pyramidal cells can have detectable effects on other neurons and even behavior. Extending these results, we show that single cortical PNs can trigger, with only one to three spikes, distributed patterns of firing that cascade across neurons, space, and time in the form of reliable firing sequences. These sequences share striking similarities with those produced during replay events in mammalian hippocampus (Diba and Buzsáki, 2007; Foster and Wilson, 2006; Nádasdy et al., 1999) and in song-generating circuits in zebrafinch high vocal center (HVC; Hahnloser et al., 2002; Long et al., 2010). They also resemble hypothesized phenomena ("synfire" chains, polychronous groups) (Abeles, 1982, 1991; Bienenstock, 1995; Izhikevich, 2006) for which experimental evidence is inconclusive (Abeles et al., 1993; Oram et al., 1999; Prut et al., 1998). Our results provide direct evidence for chained synaptic activation in a cortical structure.

RESULTS

We used *ex vivo* slabs of turtle dorsal cortex, a three-layered visual cortex transcriptomically related to neocortex (Tosches et al., 2018), patch-clamp and micro-electrode array (MEA)

recordings (Figure 1A), and optogenetics (STAR Methods) to examine multi-scale cortical connectivity. From MEA experiments, we sorted hundreds of extracellular units, classified as excitatory (E) or inhibitory (I), using their spike-induced fields (SIFs) or pairwise correlations (Shein-Idelson et al., 2017). We recorded from both PNs and interneurons, but the majority of MEA-recorded units were interneurons. This bias is due to the physical proximity of interneurons to the MEA surface (Figure 1A). Among the ~25,000 neurons/mm^2, only ~7% are interneurons (C.M. Müller, personal communication). Given this sampling bias, we probably detected <1% of the PNs but up to 30% of the interneurons in the sampled volume.

Minimal Stimulation of Single Pyramidal Neurons Generates Reliable Sequences

Baseline firing rates in turtle cortex *in vivo* are 0.03 [0.02, 0.09] spk/s (median [25th, 75th percentile]; n = 1,704 units, 4 animals) (Fournier et al., 2018). Baseline rates in the slab were 0.01 spk/s (E: [0, 0.05] n = 100; I: [0, 0.04] n = 827; 3 experiments) and irregular but occasionally interrupted by brief bursts of activity (Figure 1B); here, the PN underwent a "spontaneous" depolarization, coincident with the activation of MEA recorded neurons. These events occurred infrequently, providing a clean and stable baseline to examine the effects of activating a single PN by current injection. This manipulation triggered activity in many other neurons in the slab (Figure 1C) (>80% of experiments). We thus examined the influence of single PNs on their surround.

Typically, one PN was depolarized just above threshold by current injection (Figure 1C). Note here that the current-induced PN spike train was interrupted by a compound inhibitory postsynaptic potential (IPSP) after only two action potentials (Figure 1C, membrane potential [V_m], inset), implying feedback inhibition. In Figure 1C, we show 45 I and 13 E units among the >270 sorted (STAR Methods). They all produced at least one action potential (AP) during the illustrated epoch. Population firing rate increased immediately upon firing of the patched PN (Figure 1C). Six of the I-units shown were reciprocally connected to the patched PN, as revealed by time-locked IPSPs (e.g., stippled lines, Figure 1C), spike-triggered averaging of the intracellular membrane current (I_m) using spontaneous APs from the interneurons, or both (Figure 1D). Hence, 1 or 2 APs produced by a single PN can (1) activate many other cortical neurons and (2) cause inhibitory feedback strong enough to interrupt spiking in that PN. We found no evidence of electrical or dye coupling between PNs from electrophysiological and intracellular-labeling experiments with hundreds of patched neurons. We therefore attribute the effects illustrated in Figure 1C to the sole influence of the recorded and depolarized PN.

From this experiment, we selected 14 MEA-recorded units (Figure 1E) based on the reliability of their response to the patched PN (STAR Methods; Figures S1A–S1F). We called a neuron's response to PN activation reliable when that neuron's firing rate (FR) exceeded baseline FR by 1 SD during a time window (2 s for long pulses and 160 ms for short pulses) (see STAR Methods; Figures S1E and S1F). We refer to these reliably activated units as "followers." The spikes of the followers spread over many tens of milliseconds from PN firing time onset (Figure 1E, top). However, after trial averaging (locked to the first evoked AP of the patched PN), the response-onset time of each follower proved to be very reliable. We thus rank-ordered the neurons according to those onset times (Figure 1F) and retrospectively applied this rank ordering to all trials (Figure 1E, bottom). Figure 1G shows the first spikes of each unit ordered as in Figure 1F over 10 trials, illustrating the sequential activation and inter-trial variability (see also Figure S1H). Although the rank of each follower varied slightly from trial to trial, some followers (especially those responding early) fired reliably in distinct and narrow time windows (discrete distributions of spike times, Figure 1H).

Given the effectiveness of two APs from one PN in generating observable effects in other neurons, we shortened the current pulses to 20–50 ms. These experiments were repeated with 40 randomly selected L2 PNs, patched in 22 cortical slabs. Followers were detected in 80% of these experiments.

Activation Sequences Evoked by Single Pyramidal Neurons Last up to 200 ms

The number of followers varied between 1 and 33 (see also Figure S2A). A single PN AP was often enough to trigger a sequence, but the number of followers increased with the number of PN APs (e.g., Figures 2A, 2B, and S2C–S2G). In each experiment, we sampled only a small fraction (300–1,000) of the ~25,000 neurons overlaying the MEA. Hence, the true numbers of followers likely exceed our measurements by several fold for interneurons (because interneuron sampling was dense [see above]) but possibly 100-fold for PNs (because we sampled <1% of them). Note also that our selection criteria for follower-neuron identification (STAR Methods) were based on firing-rate-increase reliability. Hence, other MEA-recorded units may have been affected by the PN, but were not included because below our acceptance threshold. Our results thus underestimate true activation.

Figures 2A–2D illustrate some features of follower activity: (1) activation is sequential (Figures 2A–2D); (2) recruitment increases with PN AP number (Figures 2A, 2B, and S2C–S2G; $r = 0.99$, $p = 0.005$, $n = 34$); (3) activation onset can be sharp, even after long delays (Figure 2D); and (4) evoked activity tends to be more prolonged in late- than in early-activated followers (Figures 2C, 2D, S2D, and S2E; correlation between median first spike time and half-width at half-height of the post-stimulus time histogram (PSTH): $r = 0.56$, $p < 10^{-21}$, $n = 245$). Figures 2E and 2F shows the spike-onset distributions of 16 and 33 identified followers from two experiments. More I- than E-units were found, but both types fired at any time along the sequence (Figures 2E and 2F). The reproducibility of sequential activation (e.g., Figures 1F–1H and 2D–2F) was confirmed using an entropy-based measure (Figure 2G). We calculated the normalized entropy for the identity of the nth AP (rank) in all trials (Figure 2G, black) and compared it to that in shuffled sequences (Figure 2G, red). Of 34 PNs that had followers, 17 showed reproducible spike sequences that were significant for orders spanning 2 to 16 followers (STAR Methods). For experiments with $\geq$10 followers (n = 9), spike ranks above 7 became indistinguishable from sequences produced by chance (Figure 2H). To illustrate the range of observed activation delays, we combined the responses of

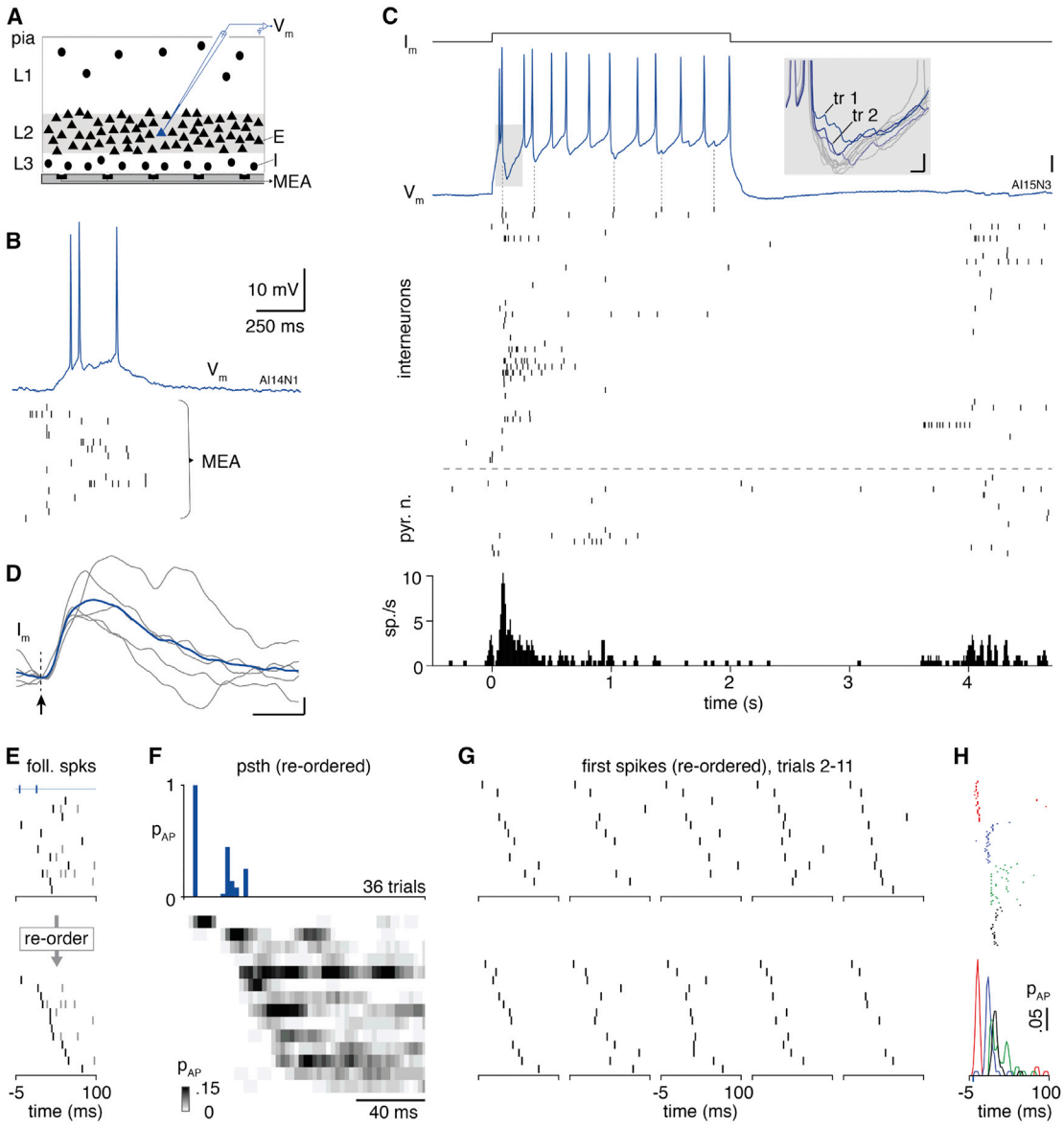

Figure 1. Single Pyramidal Neurons Generate Reliable Sequential Activity

(A) Scheme of recording configuration. E, excitatory neuron; I, interneuron; MEA, microelectrode array; L1–L3, layers 1–3.

(B) Spontaneous activity recorded with intra- (V_m) and extra-cellular (MEA) methods. 17 units fired at least one AP during this epoch. V_m, membrane potential. See also Figure S1G.

(C) Activation of one PN (V_m) by current injection (I_m) activates other neurons. V_m calibration as in (B). Inset: overlay of 10 successive trials showing IPSPs; trials (tr) 1–3 are in blue. Note augmentation of hyperpolarization over early trials. Calibrations: 5 mV, 20 ms. Vertical stippled lines denote linked interneuron and IPSPs (see D). pyr. n., pyramidal neurons. Bottom: population PSTH.

(D) Single (gray) and averaged (blue) I_m of the PN in (C) in voltage-clamp mode, triggered on spontaneous APs of topmost I unit in (C). $V_{hold} = -50$ mV; arrow, time of AP trigger. Calibrations: 10 pA, 10 ms.

(E) Followers (see text) are activated in sequence. Top: single-trial spike raster of followers in (C). 12 of 14 followers active during this trial. Blue tick marks represent PN APs. Followers: first-spikes are in black, and the others are in gray. Bottom: raster after rank ordering by first-spike time. See also Figures S1A–S1F.

(F) Normalized PSTH of patched PNs (top, blue; trigger on first PN AP) and followers (bottom). Follower PSTHs color-coded by AP probability per time bin and ordered by median first-AP time.

(G) Successive trials of first-AP raster, ordered as in (F). Median number of active followers per trial, 12. See Figure S1H for rasters with all APs.

(H) Top: first-AP rasters of four followers (four colors) over 36 trials. Bottom: first-spike PSTH of these followers (smoothed with 6-ms sliding average). Foll. 1 (red), $p_{AP} = 0.9$ at 4 ms [4, 6] (median first spike time, [25th, 75th percentile]); Foll. 2 (blue), $p_{AP} = 0.97$ at 20 ms [18, 24]; Foll. 3 (green), $p_{AP} = 1$ at 34 ms [24, 44]; Foll. 3, divided into early and late spike windows, $p_{AP < 35ms} = 0.5$ at 24 ms [24, 30] and $p_{AP >35 ms} = 0.5$ at 44 [42, 49]; Foll. 4 (black), $p_{AP} = 0.63$ at 28 ms [26, 31]. The probability and timing of the second intracellular AP was $p_{second\ AP} = 0.97$ at 16 ms [14, 18].

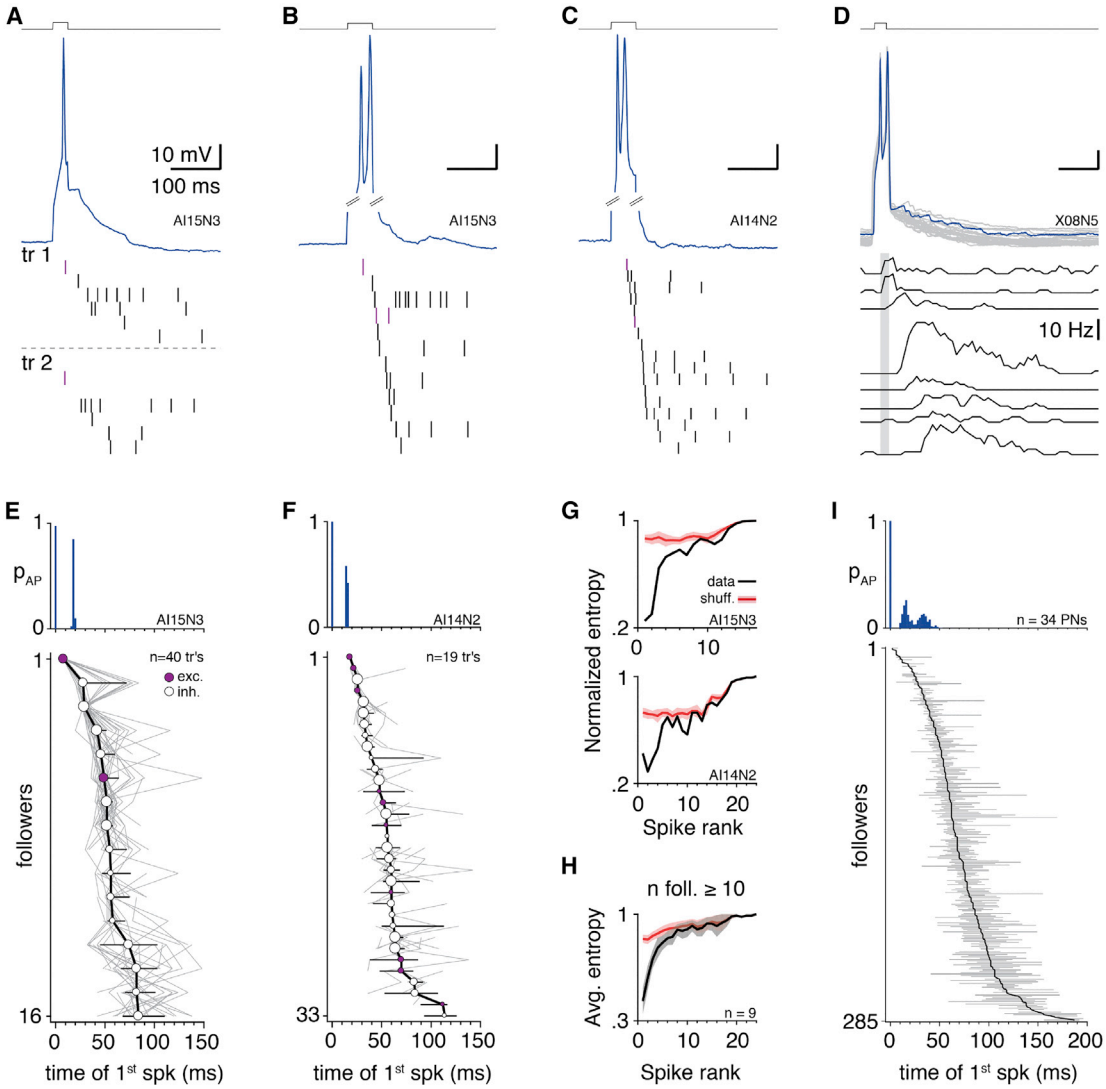

Figure 2. Activation Sequences Evoked by Single PNs Last up to 200 ms

(A) Follower sequence evoked by one AP in a patched PN (same as in Figures 1C–1H). Short direct current (DC) pulse (400 pA, 30 ms) evokes a single AP in a PN (middle). Bottom: follower-spike rasters from trials 1 and 2 (n = 6 followers). Same rank ordering of followers in trials 1 and 2. E-sorted units, magenta; I-sorted units, black.

(B) Two PN APs lead to increased follower recruitment. Same PN as in (A) but with longer current pulse (50 ms); 12 followers, one trial. See also Figures S2C–S2G. Calibration as in (A).

(C) Same experiment as in (B) but with a different PN. Seventeen followers were activated in this trial (33 in total for this PN). Calibration as in (A).

(D) Same experiment as in (B) and (C) but with a different PN and follower responses shown as PSTH over 26 trials (10-ms bins). All traces aligned to time of first PN AP. Gray bar marks the window between the first and second PN spike. Note the sharp averaged onset of even the latest-activated follower and longer activation of late-activated followers. V_m calibration as in (A).

(E) Reliable sequential follower activation outlasts current-induced spike doublets in PN. Top: normalized PSTH of patched PN APs (40 pulses, same PN as in B). Median time of PN's second AP: 18 ms. Bottom: followers ordered according to median time of first-AP across all trials. First-spike times for all trials are plotted in gray for each follower. Followers first-spike times are connected by line if the next-in-order follower is active during that trial. Circles, error bars: median first-spike time, 25th and 75th percentile. Circle size: reliability. Magenta: presumed E (from spike induced field).

(F) Same as (E) for the experiment in (C). Median time of PN's second AP, 14 ms.

(G) Top: normalized entropy of sequence for the experiment in (A) and (E). Bottom: normalized entropy of sequence for the experiment in (C) and (F). Black, data; red, average of 100 shuffled sequences.

(H) Average normalized entropy of n = 9 experiments with ≥10 followers (see STAR Methods).

(I) Follower sequences last up to 200 ms. Top: normalized PSTH of 34 patched PNs. Bottom: median and 25th and 75th percentile of first-AP time of the 285 followers activated by the 34 PNs, for pulse number 7 of a pseudo-random pulse protocol (see STAR Methods). Followers are ordered by rank, independent of the experiment in which they were recorded.

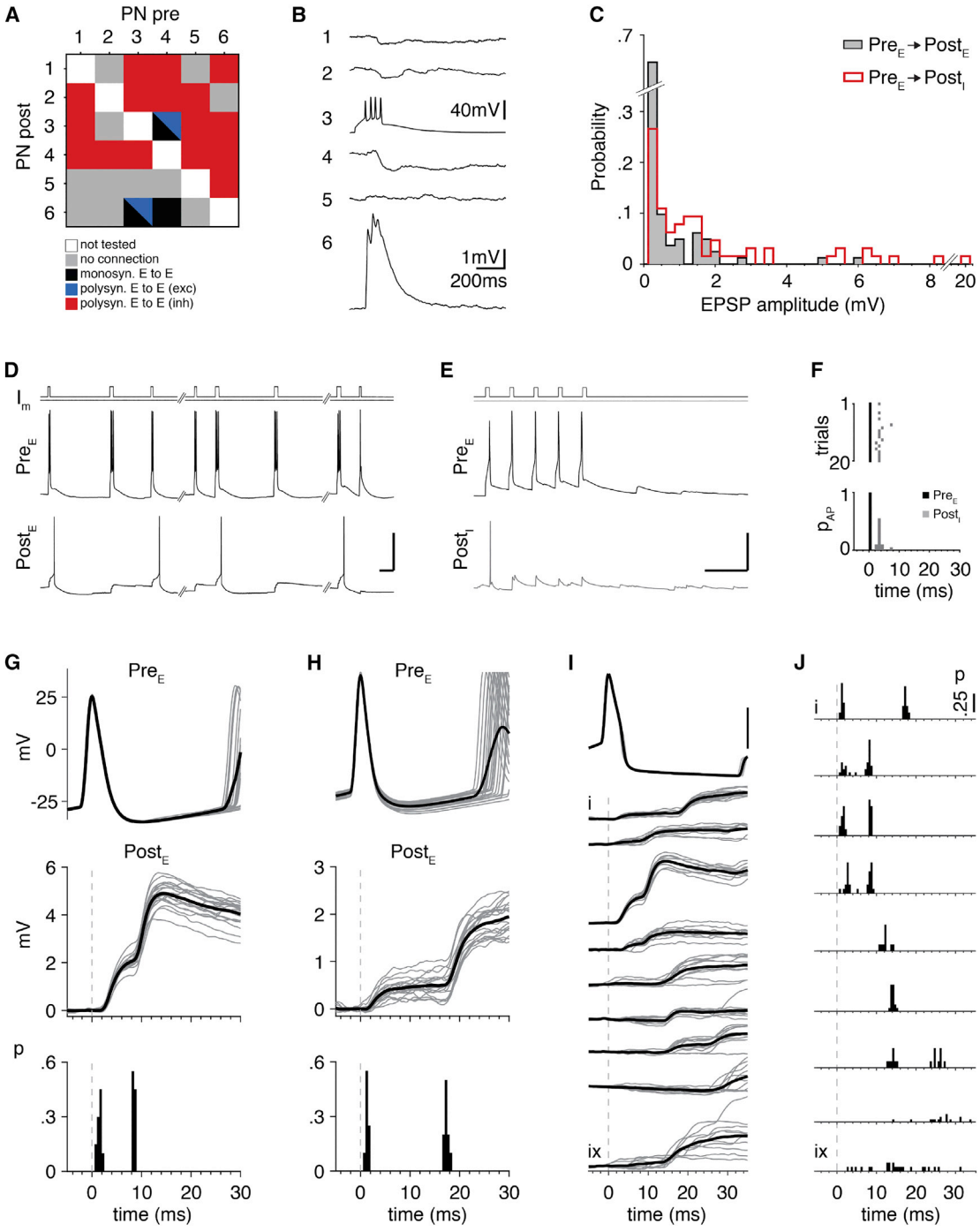

Figure 3. Intracellular Recordings Reveal Reliable Polysynaptic Transfer

(A) Connectivity matrix of six simultaneously recorded PNs. Bicolor squares represent a combination of monosynaptic and polysynaptic excitation. See also Figures S3A–S3D.

(B) Test of output connectivity of PN_3 (third column in A). PN_3 activated by DC pulse; V_m traces of five other PNs aligned to first AP of PN_3 and averaged over 20 trials. PN_3 made at least four connections onto other PNs (1, 2, 4, and 6), three of which (1, 2, and 4) were indirect and inhibitory. Vertical calibration of 1 mV applies to subthreshold V_m of PN_1–PN_2 and PN_4–PN_6.

(C) EPSP amplitude distribution is heavy tailed. EPSP amplitude histogram pooled across direct EPSPs onto excitatory (n = 77) and inhibitory (n = 64) postsynaptic targets.

(D) Spike transfer between PNs. Suprathreshold current pulses of variable duration (I_m) applied to Pre_E alone (top). Note consistent EPSP in $Post_E$, reaching AP threshold in four of eight pulses. Mean unitary $Post_E$-EPSP amplitude: 6 ± 1 mV (n = 24 trials). Note the slow EPSP decay time. Calibration: vertical, 40 mV; horizontal, 200 ms.

(legend continued on next page)

285 followers recorded over 34 experiments (Figure 2I), rank-ordered by response onset and aligned to the time of the first current-evoked AP in their respective patched PN. Follower-response onsets spread over 190 ms, with most onset times after the last current-evoked PN spike time (median = 26 ms, SD = 9 ms).

We used a measure based on pairwise rank correlations (STAR Methods) to quantify the similarity of rank ordering across trials of each follower relative to all other followers (Figures S2H–S2K). Sequence reliability far exceeded that for shuffled sequences and remained high throughout a sequence. Restricting this analysis to nearest neighbor (NN) segments of a sequence revealed that (1) reliability decays over time (neurons that fire early have a more consistent rank than ones that fire late) and (2) temporal decay of reliability is stronger for small than large NNs, indicating that global ordering is more stable than fine ordering.

Intracellular Recordings Reveal Reliable Polysynaptic Paths

Local Connectivity

Our results suggest that excitatory synaptic coupling must be reliable and dense enough to trigger chained activation of cortical neurons. To estimate direct and indirect connection probabilities, we carried out simultaneous, visually guided patch-clamp recordings from multiple neurons in 3 × 4-mm slabs. We patched over 400 neurons in simultaneous sets of 2–8, with inter-cell distances of 136 ± 110μm (mean ± SD), ranging from 6 to 722 μm, and tested 913 possible monosynaptic connections (Figure 3). Resting potentials were −65 ± 8 mV (E, n = 128) and −63 ± 9 mV (I, n = 43), and firing thresholds were −37 ± 8 mV (E) and −37 ± 10 mV (I). Probabilities of direct connection (STAR Methods) were E-E: 77/595, p_{EE} = 0.13 [0.10, 0.16]; E-I, 64/140, p_{EI} = 0.46 [0.38, 0.54]; I-E: 69/140, p_{IE} = 0.49 [0.41, 0.57]; and I-I: 10/38, p_{II} = 0.26 [0.12, 0.40] (Figure S3A; [x, y]: 95% confidence interval estimated from a binomial distribution). I-E connection probability, measured separately between MEA-recorded interneurons (L3) and patched PNs, was p_{IE} = 0.4 [0.2, 0.6] locally (Figures S3B and S3C). Assuming independence, these numbers suggest a probability of indirect inhibitory connectivity between any two PNs of ∼0.2 (p_{EI} × p_{IE}). The measured rate of indirect inhibition between PNs was 0.37 [0.33, 0.42] (146/391 pairs), suggesting that reliable connection paths exist in addition to the shortest ones.

Spatial Distribution of PN-PN Connectivity

Most of the direct E-E pairs were found within a radius of 250 μm. Although PN axons extend very widely, often well beyond 1 mm from the soma, we found only one distant connected pair, with a soma separation of 580 μm, reflecting PNs' declining axon collateral density with distance. By contrast, the probability of indirect inhibitory connections between PNs was low for neighboring PNs and grew to ∼300 μm (Figure S3D), suggesting a "Mexican hat" profile of average local interactivity (E and I) between PNs (Couey et al., 2013). Note that our estimates of connection probability are more reliable within a radius of 350 μm, due to denser sampling of pairs within that radius.

Direct and Indirect Evidence for Polysynaptic Connectivity

Polysynaptic interactions are extremely common in this cortex. In the PN sextuplet in Figures 3A and 3B (the six PNs were patched randomly), each neuron influenced (mostly indirectly) at least one and sometimes all the others. PN_3, for example (depolarized by current pulse injection; Figures 3B and 3G), provided direct monosynaptic excitation to PN_6 and inhibited indirectly PN_1, PN_2, and PN_4. Among 200 neurons recorded in sets of more than four neurons, 192 (96%) had at least one detectable mono- or poly-synaptic (pre-, post-, or both) partner in the set. Because each set was small and selected randomly among 25,000 neurons/mm^2, local connectivity must be high and include connections reliable enough to ensure polysynaptic transfer. Consistent with this, the amplitude distribution of monosynaptic excitatory postsynaptic potentials (EPSPs) onto PNs and interneurons was heavy tailed (Figure 3C; bias-corrected skewness = 5.3); some excitatory connections were indeed strong enough to fire postsynaptic targets (E or I) with single or pairs of presynaptic action potentials (Figure 3D for E-E; Figures 3E and 3F for E-I). Threshold crossing was probably aided by depolarizing voltage-dependent nonlinearities activated by EPSPs. Because sequences (as in Figure 2) could be initiated from the great majority of randomly selected PNs, we conclude that most PNs must contain, among their thousands of output synapses, at least a subset of strong ones.

Evidence for Reliable, Delayed, Unitary Excitatory Synaptic Potentials

Single PN action potentials reliably produced excitatory synaptic potentials in a target neuron with short and reliable latency (E-E delay from spike time to EPSP onset: 1.5 ± 3 ms, n = 77 pairs; E-I delay: 1.2 ± 1ms, n = 64 pairs), consistent with monosynaptic connections (Figures 3G and 3H). The same action potentials, however, often caused in the same postsynaptic neuron or a different one EPSPs with a longer yet equally reliable latency (e.g., after 8, 18, or 26 ms) (Figures 3G–3J and S3E–S3G), even though the source PN had fired only once. The latency and jitter of the first and second EPSPs in Figure 3G were

(E) Spike transfer between PN and interneuron. Same as (D) but with postsynaptic interneuron ($Post_I$). Calibration as in (D).
(F) Same pair as in (E), showing APs only (responses to pulse 1 of 5, as in E, over 20 trials). Pre-post AP delay = 3.7 ± 1 ms (16 post-APs in 20 trials).
(G) Direct evidence for polysynaptic potentials. Top to bottom: Pre_E V_m (PN_3 in A), $Post_E$ V_m (PN_6 in A), $Post_E$ EPSP-onset time histogram. Note reliable and precisely timed (peak p = 0.5 per 0.5-ms bin) EPSP onsets at 1.5 ± 0.5 ms (monosynaptic) and 8.5 ± 0.2ms (polysynaptic).
(H) Same as (G) but for pair Pre_E4-$Post_E3$ in (A). EPSP onsets: 1.4 ± 0.3 ms (monosynaptic) and 17.5 ± 0.4 ms (polysynaptic). For divergent connections from one Pre_E to one $Post_E$ (mono- and polysynaptic) and one $Post_I$ (monosynaptic), see Figures S3E–S3G.
(I) Illustrative examples. Top: representative presynaptic AP, to indicate time trigger. Bottom: 9 mono- and/or polysynaptic connections (10 trials each) ordered by delay to first EPSP. Calibration: 40 mV for AP, 4 mV for EPSPs. i–viii, E-E pairs; ix, E-I pair.
(J) EPSP-onset time distributions for data in I (i–ix). See Figures S3H for cumulative histogram and Figure S3I for autocorrelation of cumulative histogram, with a 6- to 8-ms period.

1.5 ± 0.5 ms and 8.5 ± 0.2 ms, respectively. The latency and jitter of the first and second EPSPs in Figure 3H were 1.4 ± 0.3 ms and 17.5 ± 0.4 ms, respectively. Those long-latency EPSPs must be polysynaptic and due to the reliable activation of one or more interposed (but not recorded) PNs. The percentages of trials in which each type of EPSP was detected were 85% ± 15% (range, 60%–100%) for monosynaptic and 98% ± 4% (range, 90%–100%) for polysynaptic EPSPs (n = 5 connections). A polysynaptic EPSP could occur even in the absence of a monosynaptic one preceding it (Figure 3Iv–viii). Polysynaptic EPSPs were on average larger than monosynaptic ones by 0.6 ± 0.3 mV. Amplitude correlation between successive EPSPs was low (r = −0.07 ± 0.3 [range, −0.5 to 0.3], n = 5). EPSP onset jitter was 0.7 ± 0.3 ms for monosynaptic and 0.5 ± 0.3 ms for polysynaptic EPSPs. Onset delays of first and secondary EPSPs were not correlated (r = −0.03 ± 0.2 [range, −0.15 to 0.4], n = 5).

Selecting for polysynaptic connections with reliable latencies, the distribution of EPSP-onset latencies across recorded pairs was multimodal, with intervals of 6–8 ms (n = 8 E-E and n = 1 E-I connections; Figures 3J and S3H), consistent with the sum of chemical synaptic delay, postsynaptic integration (EPSP rise time-to-peak; E-E: 5 ± 6 ms, n = 77 pairs; E-I: 3.9 ± 2 ms, n = 64 pairs), and AP rise time in interposed neurons. Mean PN axonal conduction velocity in this preparation is ~150 μm/ms (Shein-Idelson et al., 2017) (i.e., too high to explain delays longer than a few milliseconds; see spatial distribution below). Also, when a single PN spike caused a double EPSP in one target neuron, failures could occur at the first or the second EPSP, independently of one another (e.g., see Figures 3I and S3E–S3G), consistent with the hypothesis that consecutive EPSPs in a target neuron are not caused by the same presynaptic spikes. Thus, one or more non-recorded PNs were interposed between the constituents of these recorded pairs. In conclusion, excitatory synaptic coupling is dense and contains high-gain connections that enable even single action potentials to propagate through multiple synapses in apparent steps of 6–8 ms, at least in the first 30 ms of polysynaptic activation.

The Temporal Features of Sequential Activation Indicate Branched Synaptic Chains

Simulation and theoretical studies suggest that the propagation of activity through a chain of connected neurons should, depending on model parameters, see either growing spike jitter along the chain or progressive synchronization (Diesmann et al., 1999; Kumar et al., 2010). We measured, for each follower, firing-onset jitter as a function of firing-onset time. We show three examples (Figures 4A–4C) and plot the relationship between jitter and delay for all recorded followers and pulse series (Figure 4D). The trend over the population (Figure 4D) indicates a positive correlation between delay and jitter.

A careful examination of individual experiments, however, revealed interesting deviations. First, certain followers showed high firing reliability and low jitter (p_{AP} = 0.97 with 8-ms jitter for the blue cell in Figure 4B; or p_{AP} = 0.78 with 17-ms jitter for the green cell in Figure 4C), even when their firing onset occurred late (Figures 4A–4D). This suggests that some of the polysynaptic routes to activation must be very reliable, consistent with intracellular data. Second, a follower responding early to a PN could be more jittery than one responding later (e.g., Figures 4A and 4C). This suggests that their activation paths must be at least in part independent of one another (e.g., one short, via unreliable connections; one long, via reliable connections), indicating divergence along activation chains. The related case of equal delay but different response jitter (Figure 4B) suggests synaptic paths of equal length but differing reliability. Third, the response-onset times of some followers (e.g., red Figure 4C) could form two successive modes. This suggests that the same neuron can be activated by partly overlapping or recurrent chains of different lengths (see also Figures S4A–S4C).

Patched PNs often reflected in their own membrane potential the synaptic consequences of the follower activation that they had triggered (Figures 1C, 2C, and 2D), indicating circuit recurrence. We used these long-lasting membrane potential fluctuations, often periodic (~10–20 Hz), to measure the phase—thereby revealing the potential synchronization—of the APs in followers (Figure 4E). This analysis was possible only late within evoked follower activity (i.e., after unfolding of the sequence proper) because (1) sequence evolution often overlapped with current-pulse-induced V_m depolarization and spiking and (2) at their onset, sequences typically evolved faster than the detectable subthreshold voltage fluctuations in the source PN. Thus, early first-spike sequences (seen over the first 200 ms) and later sustained activity had different temporal signatures. In each experiment, some followers were locked to V_m (e.g., followers 1–3, top row, Figure 4F) while others were not (e.g., followers 4–6, bottom row, Figure 4F). In aggregate, however, followers were locked to the same phase of V_m, before the oscillation peak at 0 rad (Figure 4G, top). Hence, late during activation, followers tended to synchronize with one another (Figure 4G, top). We performed this analysis in seven experiments that showed clear and reproducible subthreshold V_m oscillations and obtained identical results (Figure 4G, bottom). The synchronized followers were mostly interneurons; because interneurons represent ~7% of the neurons in turtle dorsal cortex and because they are heavily connected locally (see above), they are probably, owing in part to their drive from PNs, the dominant cause of this synchronization and of the subthreshold V_m oscillations detected in the PNs.

We then examined temporal correlations between followers as further potential signs of chained activation. We selected two experiments in which at least one of the recorded followers was another PN (Figures 4H and S4D–S4F). In this example (Figure 4I), the patched PN activated 33 followers, of which three are shown (F1–F3). F1 was another PN, and F2 and F3 were interneurons, whose firing onsets were synchronous with one another but delayed relative to F1. We have no evidence for any direct connection between PN, F1, F2, and F3. Figure 4I shows the PSTHs of the four neurons triggered either on the last spike of the depolarized PN, source of this sequential activity (top row), or on the spike of F1 (bottom row), first element in the sequence downstream of the PN. Shifting the trigger to F1 had the effect of sharpening the PSTHs of F2 and F3 (bottom row, Figure 4I). This indicates that the firing times of some followers are not independent of one another, supporting the hypothesis of chained paths (see also Figures S4D–S4F). In a group analysis (26 experiments; STAR Methods) we found that tightening of the

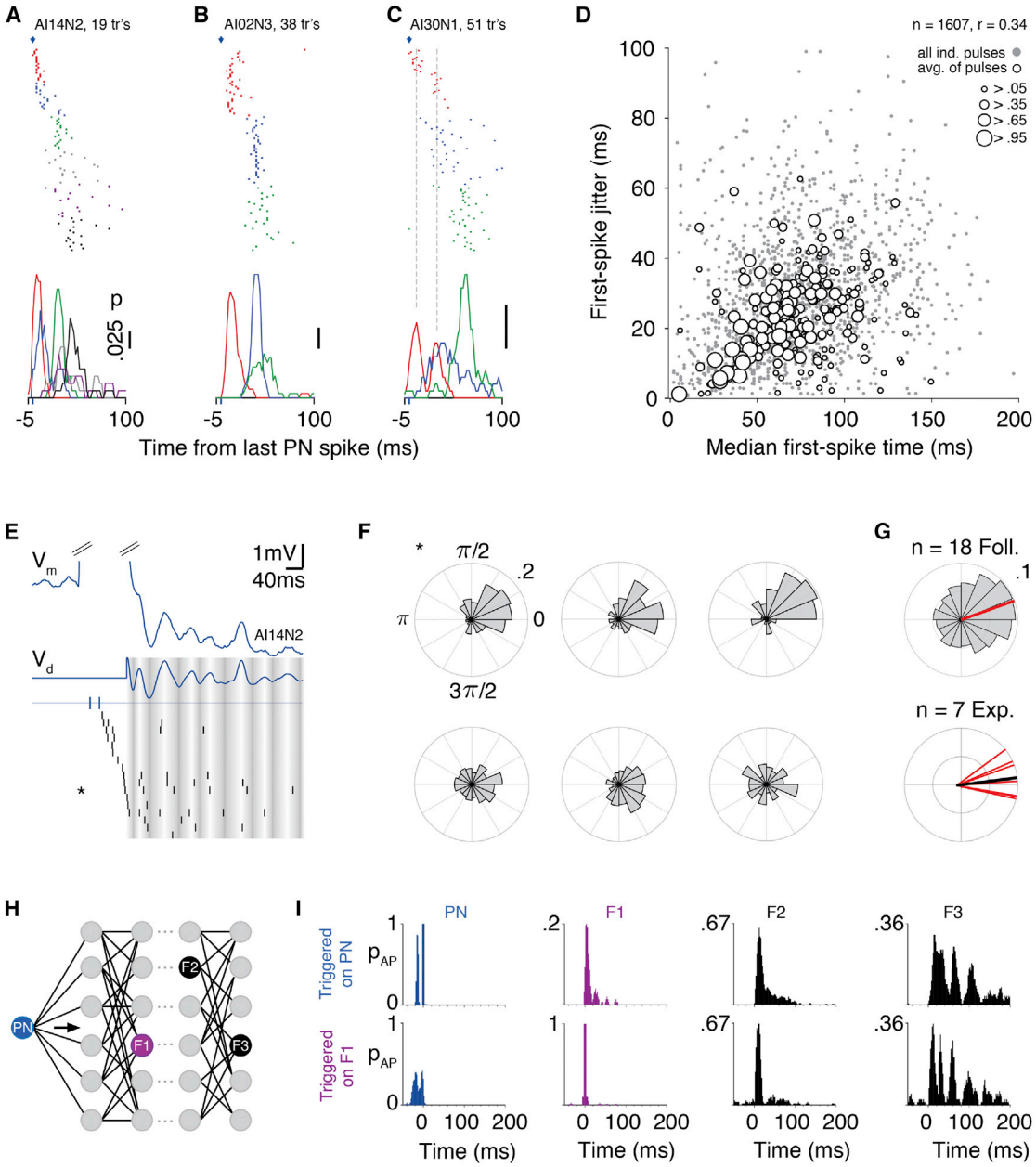

Figure 4. Temporal Features of Sequential Activation Indicate Branched Chains

(A–C) Top: first-spike rasters for six (A) or three (B and C) followers, aligned to time of last PN spike (arrow). Bottom: smoothed follower PSTHs, as in Figure 1H. Note bimodal firing time of red follower in (C) (stippled lines). Calibrations as in (A). See also Figures S4A–S4C.

(D) Jitter of follower-onset grows with onset delay. Gray dots, all pulses (within and across pulse trains, n = 1,607). Open circles, averages over pulses in a train (n = 250 followers; see STAR Methods). Open circle size, average firing probability per follower (see legend). Note followers with late firing onset but low spike-time jitter.

(E) Followers are phase-locked to subthreshold V_m fluctuations of PN. V_m, membrane potential of patched PN in (A); V_d, filtered and de-trended V_m (see STAR Methods); blue tick marks, AP times of patched PN; below, follower raster. Asterisk indicates the follower shown in (F). V_m fluctuations, white (peak, 0) to dark (trough, π rad).

(F) Histograms of follower-spike phase relative to V_m. Followers are from the experiment in (E) (see text).

(G) Top: AP phase histogram pooled over 18 followers that fired >50 times during the repeated protocol in (E). Mean phase in red. Bottom: mean follower-firing phases for seven experiments in which the patched PN displayed subthreshold fluctuations (red). Average across experiments in black.

(H) Cartoon of hypothetical network supporting branched synaptic chains (see I).

(I) Top row, from left to right: normalized PSTH of patched PN (same as in A and E–G); F1–F3, PSTHs of followers F1 (a PN) and F2-F3 (both interneurons). Top row: F1–F3 responses aligned to last AP of PN. Bottom row: PN and F2-F3 responses aligned to F1 spikes. Note sharpening of F2-F3 PSTHs in the bottom row, suggesting response correlation to F1 firing. Interquartile range of first-spike times were reduced from 8 ms to 4 ms for F2 ($p < 10^{-7}$, Wilcoxon rank sum test) and from 14 ms to 11 ms for F3 ($p < 10^{-5}$, Wilcoxon rank sum test). See also Figures S4D–S4F.

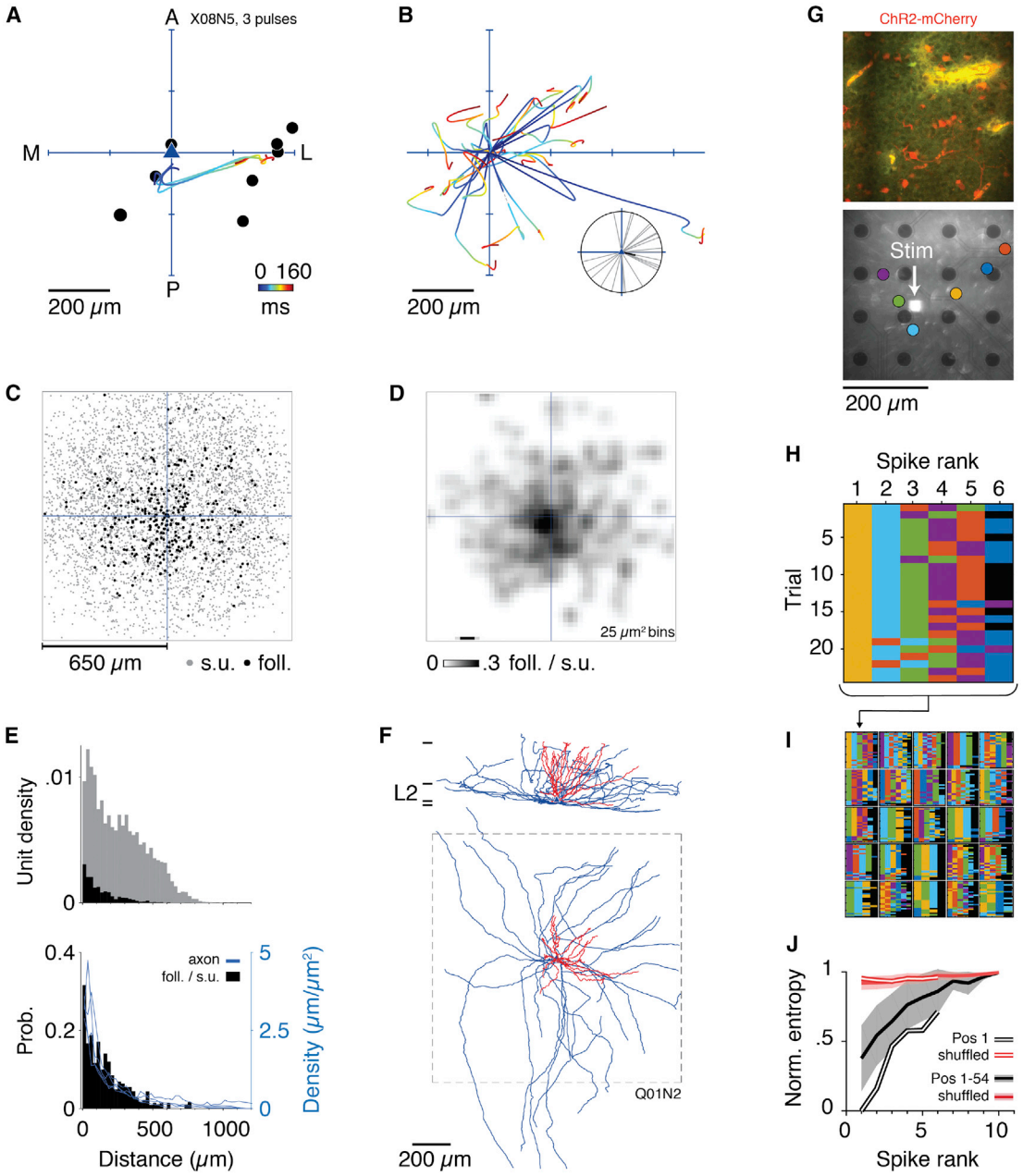

Figure 5. PN-Evoked Activity Extends over at Least 1 mm^2 of Cortex

(A) Sequential activation traces reliable physical path through cortex. Spatial evolution of follower activity traced by center-of-mass of activity over time in the tangential plane. Each example is mean over n = 26 trials, time color-coded. PN soma (blue) located at the origin. Black circles represent follower somata, determined by triangulation (n = 8). A, anterior; L, lateral; P, posterior; M, medial. Same orientation in (A)–(D) and (F).

(B) Trajectories as in (A), for 22 experiments with n ≥ 5 detected followers, with origin at center-of-mass of first-activated followers in each experiment. Distance to origin increased over time ($r = 0.81$, $p < 10^{-17}$). Inset: distribution of unit vectors representing directions from start to end of trajectory. Circular mean in black. See Figure S5A for propagation speed estimate.

(C) Position of all sorted units (s.u.; gray) and followers (foll., black) relative to position of their patched PN (center).

(D) Ratio of followers to sorted units per 25-μm^2 bin. See Figure S5B for binned version of s.u. counts.

(E) Top, s.u. and follower density (gray and black, respectively) over distance from patched PN (25μm bins). Bottom, probability of follower activation over distance. Blue lines, overlay of axonal density as function of distance from soma for 4 PNs (18–46 mm total axonal length).

(F) PN axonal arbors (blue) extend beyond 1 mm^2 (see also Figure S5C). Top: coronal view of reconstructed L2 PN (biocytin). Dendrites, red. Cortical layers indicated at left; pia up. Total axonal length, 24 mm. Bottom: same, tangential view.

(G) ChR2-induced sequences. Top: tangential view (from ventricular surface) of maximum intensity projection of upper L3 to lower L1 of a dorsal cortex slab showing ChR2(H134R)-mCherry (red) expression under a CaMKIIa promoter. Yellow signal comes from blood vessels. Bottom: light spot excitation of a cortical

(legend continued on next page)

first-spike time distribution after realignment (Figure 4I, F2 and F3; and Figure S4G) was observed with relatively few followers; most showed either no tightening or a slight dispersion (Figure S4H; median IQR change, 3 ms [−3, 12], n = 600, $p < 10^{-20}$, Wilcoxon signed-rank test). Thus, spike timing precision rarely increased over the duration of a sequence.

Single-PN Evoked Activity Extends over at Least 1 mm^2 of Cortex

Using triangulation to locate 6,389 sorted units, we tracked the spatial features of the activity evoked by each depolarized PN (n = 34, Figure 5). In each experiment, the earliest activated neurons (<10 ms) usually lay within 75 μm of the patched PN. The onset of activity then moved away in the cortical (tangential) plane, at a mean radial velocity of 15 $\mu m \cdot ms^{-1}$ ($r = 0.36$, $p < 10^{-7}$, n = 245, where r measures the correlation between median time of first AP and distance from the patched PN; as low as 8 $\mu m \cdot ms^{-1}$ in some experiments; Figure S5A), that is, 10–20 times slower than axonal AP propagation (Shein-Idelson et al., 2017).

The physical path of sequential activation was reliable over trials (Figure 5A). In all recordings, activity trajectories moved away from the PN source with time, independent of the mean direction of motion (Figures 5B and S5A; correlation between tangential distance of center of mass of activity and time for data shown in Figure 5B: r = 0.81, $p < 10^{-17}$, n = 34). Trajectories extended in all cardinal directions, with a small average positive bias toward lateral cortex and negative bias toward the antero-medial quadrant (Figure 5B and inset). Figure 5B plots trajectories from 22 experiments (more than five followers) for clarity. In aggregate, follower activation spread over the entire sampling area (i.e., 1 mm^2 centered on the PN source) (Figures 5C and 5D). We did not observe any unit sampling bias in the tangential plane (Figure S5B). Follower activation probability was high locally and decreased with distance from the source PN (Figure 5E). This range of activation was broadly commensurate with individual PNs' axonal density profiles (Figures 5E, 5F, and S5C, total axonal lengths 18–46 mm, n = 4 PNs). These results suggest that, although sequences result mostly from polysynaptic pathways, they evolve in local volumes constrained by PN axonal density. This supports earlier measurements that excitatory coupling between E-cells is strongest locally. Long-range activation of followers beyond the limits of the MEA (Figure 5E) cannot be ruled out.

Did our observations result from a recording bias toward "special" PNs? To test for such selection bias, we combined MEA recordings with a lower-precision but larger-span optical approach. We expressed ChR2 at low density in excitatory PNs (using AAV2/1-CamKIIa-hChR2(H134R)-mCherry, 3.2 ± 0.9/100 μm^2 ChR2-positive cell bodies; STAR Methods) and used a digital micro-mirror device to illuminate the recording area in 26 × 26-μm spots (Figures 5G and S5D–S5F). Because ChR2 expression was sparse (due to the low infectivity of this serotype in turtles; Pammer, 2018), each illumination spot contained on average 0.24 ± 0.06 ChR2-positive PNs. After choosing an intensity appropriate to generate just-detectable MEA activity in one spot, we tiled the recording area in a pseudo-random fashion with illumination spots (one spot at a time) in a process repeated 25 times (Figures S5D–S5F). MEA units were sorted, classified, and selected as described previously (Shein-Idelson et al., 2017). The results obtained with one illumination spot illustrate a light-evoked activation sequence of neurons, its reliability over trials (Figures 5H, 5I, and S5E), and the statistical significance of this reliability (Figure 5J). Figure 5I displays sequences (each one invoking different participating neurons) evoked by the illumination of 25 different spots, and Figure 5J tests for their statistical significance over 54 illumination sites. Whereas not all sites caused a detectable sequence (due to the absence of ChR2-positive PN or to inadequate local light intensity), more than half of them did. Cortical sequence activation is thus not a focal phenomenon or the result of bias in PN selection for patching.

Interactions between Sequences and E-I Balance

The amplification of one to three spikes into the activation of tens of neurons suggests that the coincident firing of a few PNs might quickly lead to explosive amplification. We thus examined the consequences of activating two nearby PNs (Figures 6 and S6) (n = 7 pairs). In the example in Figures 6A and 6B, the PNs (somata 150 μm apart) evoked nonoverlapping follower sequences (Figure 6B, two leftmost panels). When stimulated together, the two PNs evoked new response patterns (Figure 6B). To compare the responses to different stimulation conditions, we take the pattern of follower activation caused by $PN_1 + PN_2$ stimulation with dt = 0 as reference (Figure 6B, middle panel). The deviations of each follower from its responses in reference condition are shown in color (PN_1 alone, PN_2 alone, delay conditions; Figure 6B), and the responses of three of these followers are shown in Figures 6C–6E (followers 1, 27, and 29 are shown in Figure 6B, none of which responded to PN1 activation alone). Follower 27 (Figure 6C) did not respond to PN_1 or PN_2 activation alone (blue, leftmost panels, Figure 6B) but responded reliably to $PN_1 + PN_2$ in all conditions (white in Figure 6B, right, because activity is the same as that with 0 delay). Follower 1 (Figure 6E) also did not respond to PN_1 or PN_2 but responded reliably to PN_1-then-PN_2 activation. Follower 29 (Figure 6D) by contrast responded very strongly to PN_2 alone and least to $PN_1 + PN_2$ with 0 delay. These examples illustrate that follower activation differ

slab on the MEA. Bright-field image of slab viewed from ventral side. White square is light spot (Stim). MEA electrodes in black. Colored dots mark triangulated positions of six sorted units responding to light activation of PNs. Sequential activity summarized in (H). Top and bottom are the same slab. See Figure S5D for setup.

(H) Light stimulation recruited responses in six neurons with consistent sequential activity (spike rank) across 25 trials. Neuron ID color-coded, with sequence reliability quantified in (J). See Figures S5E and S5F for further details.

(I) Spike-rank plot as in (H) for 25 different positions of focal light stimulation. Each subplot represents a different position and a different responding subset.

(J) Quantification (normalized entropy, see STAR Methods) of sequence reliability for data in (H) (measured: open black line; shuffle control: open red line) and across 54 stimulation positions (empirical, black; shuffle control, red).

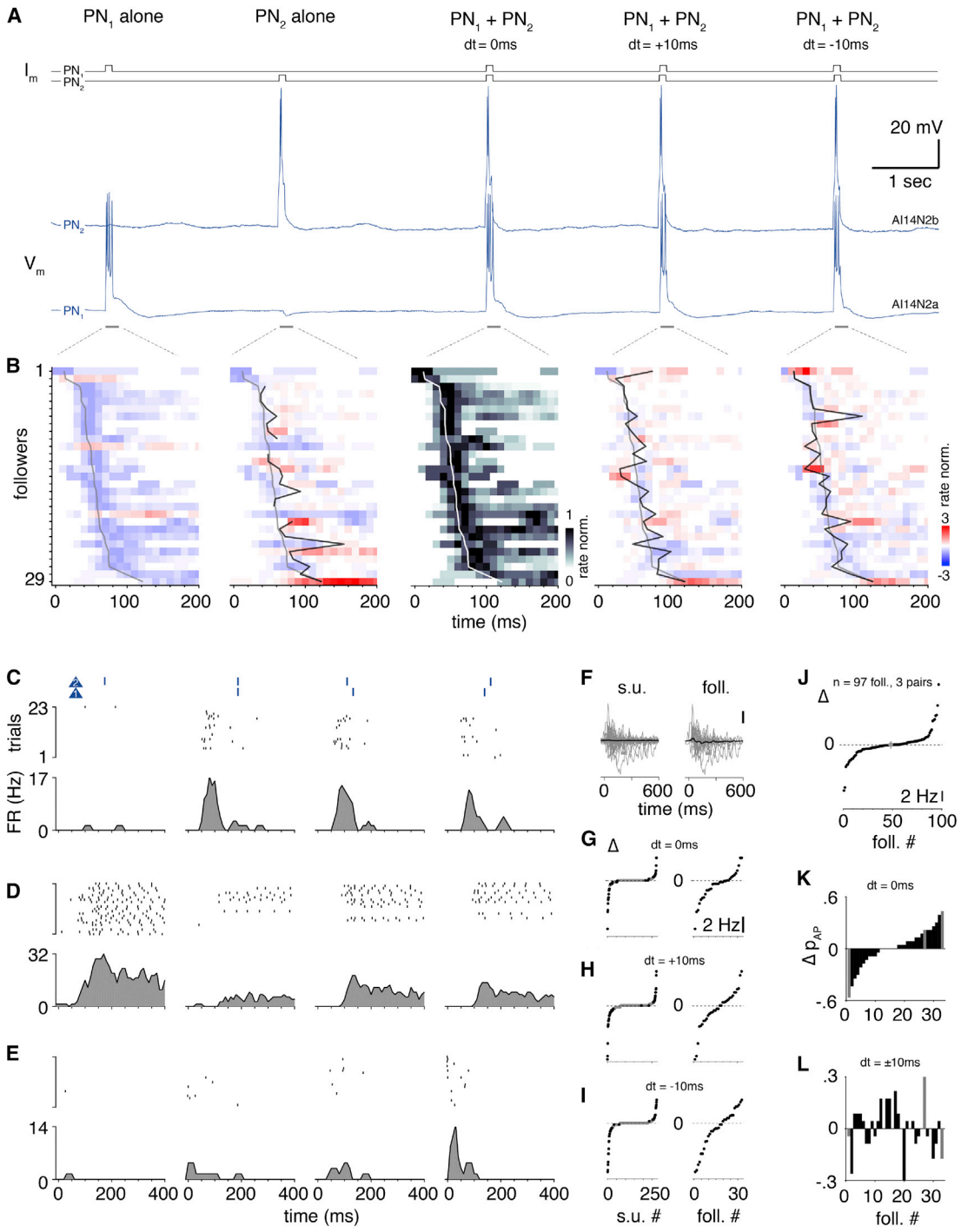

Figure 6. Sequence Collisions Reveal Balancing Interactions

(A) Coactivation of PN pair and their respective follower sequences. I_m, DC pulses into PN_1 and PN_2 and their respective V_m. Gray bars below PN_1 V_m, epochs expanded in (B).

(B) Panels show follower PSTHs in response to different activation conditions, normalized to follower peak firing rate of dt = 0 condition (middle panel). Follower order according to median first-spike time of dt = 0 condition (white line in middle panel; gray line in other panels).

(C) Top: schematic of PN activation conditions, applicable to (C)–(E). Spike raster (middle) and PSTH (bottom) of follower 27 for 4 PN activation conditions (from left to right): PN_2 alone, dt = 0, dt = +10, and dt = −10. Follower 27 showed increased activity in response to all coactivation conditions.

(D) Same as (C) but for follower 29. Follower 29 showed decreased activity in response to all coactivation conditions.

(legend continued on next page)

with PN-activation conditions and do not necessarily increase with PN recruitment. To quantify this, we measured the firing-rate difference for all sorted units (s.u.; left, Figures 6F–6I) and all followers (right, Figures 6F–6I) between their responses to each [PN_1 + PN_2]-stimulus condition and the sum of their responses to each PN stimulated alone. The net median firing rate difference caused by paired PN stimulation amounted to 0 spk/s [−0.84, 0.55] ($p = 0.37$, $n = 33$ followers; black trace, Figure 6F); increased activation of some followers was compensated for by the reduced activation of others (see also Figures 6G–6L, $p > 0.3$ for all dt conditions, Wilcoxon signed-rank test). Figures S6A–S6E shows the same analysis for another paired PN recording, and Figure 6J pools the results of three such experiments. All indicate balanced interactions (median rate change: −0.06 spk/s [−0.77, 0.64], $n = 97$ followers; $p = 0.53$, Wilcoxon signed-rank test). Spiking probability was also balanced across the follower population ($p = 0.60$, Wilcoxon signed-rank test; Figures 6K and S6D). Finally, some followers showed high sensitivity to the temporal order of paired PN activation (Figure 6L). These results indicate the absence of supralinear amplification as the number of activated sources increases from one to two PNs. Consistent with the activation of interneurons detailed above, this result reveals homeostasis in cortical activation.

To examine the influence of basal firing rate on sequences, we ran experiments with the cholinergic agonist carbachol ($n = 6$). Addition of carbachol raised average network firing rates 5-fold from 0.02 ± 0.05 spk/s (control) to 0.10 ± 0.24 spk/s (+carbachol; $p = 3.7 \times 10^{-11}$, Wilcoxon rank sum test; Figure S6F). However, the timing and probability of observing sequences ($p = 0.2$, Wilcoxon rank sum test; Figures S6G and S6K), the balancing of activity ($p = 0.62$, Wilcoxon singed-rank test; Figures S6H and S6I), and the average follower activity ($p = 0.95$, Wilcoxon rank sum test; Figure S6J) were unchanged. In carbachol, follower-count was moderately reduced (−33% ± 17%, $n = 6$; range, 11%–54%). This reduction was due to dropout of low-reliability followers and decreased sensitivity of our follower-detection criteria as baseline firing rates increased.

DISCUSSION

Pyramidal neurons in intact slabs of turtle three-layered cerebral cortex have a powerful impact on their local surrounding; one to three action potentials produced by one PN can cause the reliable sequential activation of tens (and possibly more) of "followers" over up to 200 ms and 1 mm^2 centered on the source PN. This sequential activation, schematized in Figure 7, results from synaptic transfer between neurons, revealing surprisingly reliable functional paths (virtual "grooves") for the propagation of weak activity through cortex.

Initiation, Propagation, and Control of Activity

The initiation of sequential activity by single neurons results from few very strong pairwise connections to both E and I neurons—reminiscent of "detonator synapses" in mammalian hippocampal CA3 (Henze et al., 2002) and neocortex (Lefort et al., 2009; Li et al., 2009; Peterlin et al., 2000). Once triggered, this activity spread across neurons and space, resulting in distributed E and I influence. Excitatory followers typically produced one or two APs when activated within a sequence. Because activity diverged from the source, further propagation of activity likely resulted both from strong pairwise connections and from converging weaker ones (Figure 7), thus depending on details of connectivity and timing (Diesmann et al., 1999). That some late-onset followers responded with little jitter is inconsistent with an explanation based on proximity of membrane potential to threshold. Sequences were detected because they were repeatable over tens of trials, suggesting the existence of reliable paths for the propagation of activity through cortex, determined by details of internal connectivity and synaptic weights and by conditions of activation (e.g., delays between APs of converging neurons). Whether sequences depend on past activity and synaptic plasticity is unknown but is an important next question.

Even though E-follower activation was under-sampled, follower activation could be initiated from ~80% of randomly selected PNs. Among those, we observed a spectrum of impact onto the network, with many cells activating few detected followers (<10) and few activating many (>20). Barring sampling artifacts, this suggests the existence of some highly connected neurons with unusual impact on the network (Bonifazi et al., 2009; Li et al., 2009; Song et al., 2005).

Sequential activation propagated 10–20 times more slowly than PN spikes along axons in turtle dorsal cortex (Shein-Idelson et al., 2017), ruling out spike propagation delays as the underlying mechanism. The distribution of reliable and precise polysynaptic EPSP-onset times, with quantized modes (every 6–8 ms) detected within the first ~30 ms, indicates activation of synaptically coupled chains of neurons. Although we are not aware of comparable sequences triggered by single cells in other systems, polysynaptic potentials triggered by single PNs have been observed in

(E) Same as (C) and (D) but for follower 1 showing increased activity selectively in response to the PN_1-then-PN_2 condition. None of the followers shown in (C)–(E) responded to PN_1 stimulation alone.
(F) Test for nonlinearity of follower responses to PN coactivation. Left: difference between arithmetic sum of PSTHs in response to activation of PN_1 or PN_2 alone and PSTH measured in response to PN_1 + PN_2 coactivation (with dt = 0). Gray lines, PSTH differences for 275 sorted units (s.u.). Black, average of 275. Right: same as left but with followers only. Vertical calibration: 10 Hz.
(G) Left, time-averaged firing rate difference (displayed by rank) of sorted units comparing arithmetic sum to dt = 0 condition (as in F). Gray, sorted units; black, followers. Right: same as left but for followers only.
(H) Same as (G) but comparing dt = 0 to dt = +10 condition.
(I) Same as (G) but comparing dt = 0 to dt = −10 condition.
(J) Summary of balanced follower activation for three PN pairs ($n = 97$ followers). Median and 25th and 75th percentiles are in gray. Median not significantly different from 0 ($p = 0.53$; Wilcoxon signed rank test). Increased activation of some followers by coactivation of two PNs is compensated by decreased activation of others.
(K) Change of follower spiking probability, comparing arithmetic sum to dt = 0 coactivation condition. Gray bars indicate followers 1, 27, and 29 shown in (C)–(E).
(L) Same as (K) but comparing dt = +10 to dt = −10 condition. See Figures S6A–S6E for the same analysis on another PN pair.

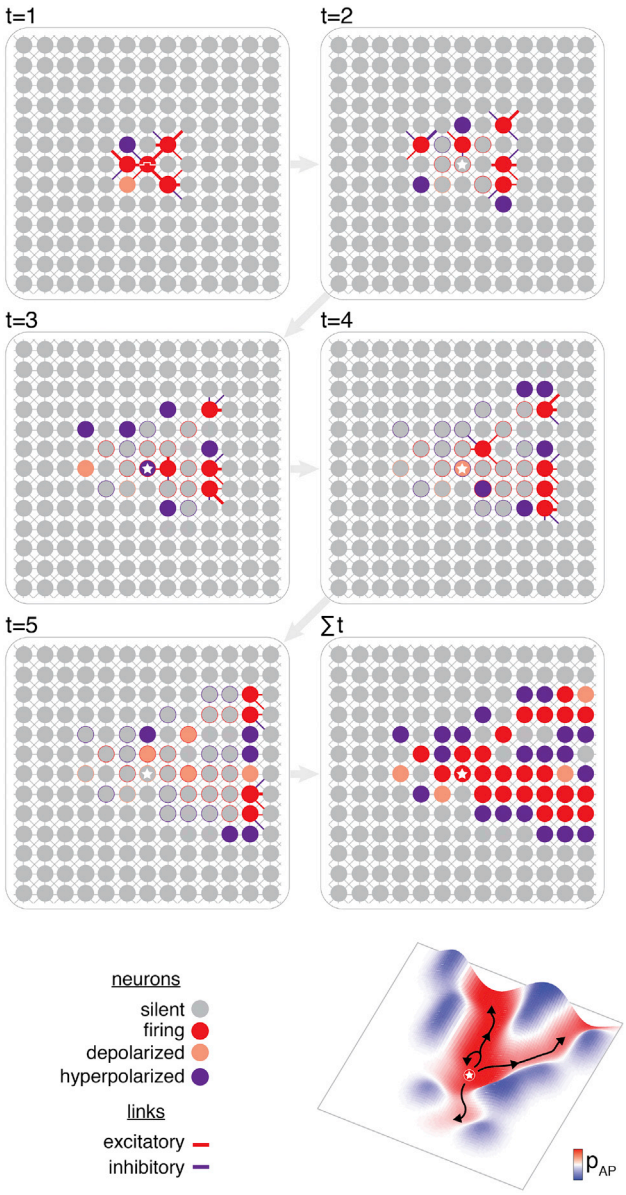

Figure 7. Schematic Summary of PN Sequential Patterns

Tangential view of idealized cortex, with only PNs represented (circles). The functional links between neurons are represented as excitatory (red, direct) or inhibitory (purple, via interposed interneurons). Activity is initiated by depolarizing one PN (center, t = 1; ★ in other frames). Its output connectivity leads to activation of a subset of first-order targets that in turn propagate activity further around them (t = 1–5). At every step, the activation of new PNs depends on the convergence of excitatory and inhibitory inputs from activated lower-order neurons. Due to recurrence within the circuit, a PN can be reactivated within the evolving pattern. Activity spreads centrifugally away from the starting neuron, invoking inhibition that sculpts virtual "grooves" of activity through the network (∑t and bottom right).

slices of human neocortex (Molnár et al., 2008). There, strong connections were found exclusively from PNs to interneurons, and excitation was propagated via depolarizing IPSPs from axo-axonic interneurons (Molnár et al., 2008), a type thus far not described in turtle cortex (Tosches et al., 2018). In rodents, single action potentials at the dentate-gyrus granule-cell mossy-fiber synapse can evoke firing of CA3 PNs (Vyleta et al., 2016), and single CA3 PN action potentials can evoke spiking in postsynaptic interneurons (Bazelot et al., 2016). Detonator synapses are thus not a peculiarity of turtle cortex.

Biological and simulated networks normally operate in a state where E and I are appropriately balanced (Berg et al., 2007; Rupprecht and Friedrich, 2018; Vogels et al., 2005; van Vreeswijk and Sompolinsky, 1996). Despite the rapid spread of activity after ignition, we never observed paroxysmal cortical activation, suggesting the selective propagation of activity within an otherwise balanced network, as proposed, for example, with neuronal avalanches (Beggs and Plenz, 2003; Eckmann et al., 2008; Lonardoni et al., 2017; Shew et al., 2015). Activity spread to small neuron groups, as evident in the small apparent overlap between follower sets activated by two different sources. After a short growth phase, activity returned to baseline within a few hundred milliseconds. The density of I coupling was likely critical in balancing local network activity. Possibly because of their small fraction in turtle cortex, L3 interneurons are both densely connected to the PN population and reliably activated during sequential patterns. They appear to control and coordinate cortical activation in a regime where activation is neither immediately shut off nor dangerously amplified. The mechanisms responsible for tuning this balance as well as the exact identity of the interneurons involved in this action are so far unknown here, but interneuron types known to play such roles in mammals, such as somatostatin (SOM) interneurons (Isaacson and Scanziani, 2011), exist also in reptiles (Tosches et al., 2018).

Functional Significance of Sequences

Single PNs caused the reliable (though not noise-free) sequential activation of other neurons. Switching the activation order of two "igniter" neurons could even generate slightly different sequences, with changes in follower rank or identity. Thus, the patterns of activation of these assemblies contained information about their cause, suggesting high combinatorial capacity (Bienenstock, 1995). The spread of activation by single PNs was constrained spatially. Although PN axonal projections are densest close to their origin, they often extend as far as several millimeters from the soma (Figures 5 and S5C; Shein-Idelson et al., 2017). If some distal connections are powerful, they could conceivably also trigger activation sequences; because our MEAs were only 1 mm^2, and because we patched neurons at the center, we could have missed such distant events.

In vivo recordings show that baseline activity in dorsal cortex is low and stimulus-evoked activity non-topographic and sparse (Fournier et al., 2018; Mazurskaya, 1973a, 1973b; Shein-Idelson et al., 2017). In cortical slabs, background activity was lower than is typical *in vivo*. Although difficult to compare to *in vivo* conditions, the carbachol results suggest that sequence generation is not an anomaly of the basal condition of cortical slabs. In an attempt to test our findings *in vivo*, we performed pilot experiments on an *ex vivo* brain preparation with eyes attached. Activation of a single patched PN (n = 1 out of 2 PNs) evoked a sequence as described here. Thus, our results may generalize to turtle brains *ex vivo*.

Visual stimuli evoke traveling waves along the latero-medial axis in this cortex in *ex vivo* explants (Prechtl et al., 1997, 2000) and *in vivo* (Fournier et al., 2018). The slight bias we observed in the propagation direction of sequences may be related to these stimulus-evoked traveling waves. Our results also lead to a reflection on the meaning of spontaneous or resting activity. If activation sequences are so sensitive to single or doublets of spikes, then why do sequences not dominate resting activity (Luczak et al., 2007)? Maybe spontaneous sequences are in fact always present but hard to detect; our discovery of sequences relied on our ability to anchor each follower's firing to the spike(s) of a controlled source (Figure S2B). Not knowing what the relevant source is when examining spontaneous activity greatly hampers one's ability to identify potential patterns.

Another hypothesis is that "spontaneous" spikes are not truly spontaneous (Luczak et al., 2009); cortical neurons are densely coupled, raising the possibility that "autonomous" neural fluctuations depend on collective population state (Pillow et al., 2008; Schneidman et al., 2006). If so, cortical circuits might be poised to selectively detect and propagate only unexpected spikes caused by an external source (such as our direct current pulses or synaptic input sources) while ignoring uninformative firings linked to collective fluctuations (Engel et al., 2001; Friston, 2010, 2018). The roles of distinct interneuron populations (Ascoli et al., 2008; Klausberger et al., 2003)—to balance or disrupt cortical activity—might be critical in such differential selectivity.

Similarity to Other Systems and Attractor Dynamics

The firing sequences we report resemble "replay" (Diba and Buzsáki, 2007; Foster and Wilson, 2006; Nádasdy et al., 1999) and "pre-play" (Dragoi and Tonegawa, 2011, 2013) sequences in rat hippocampal CA1 and song-related sequences in songbird HVC (Hahnloser et al., 2002). Although their underlying mechanisms are unknown, a prevailing model for the generation of HVC sequences consists of chains of synaptically connected neurons shaped during song learning (Long et al., 2010; Long and Fee, 2008; Okubo et al., 2015). Our results lend partial credence to such a model. Given the analogies between mammalian hippocampus and reptilian cortex (Tosches et al., 2018), CA1 replay might also be the expression of chained neural activation.

More broadly, these evoked sequences are not unlike the evolving sequences of odor-evoked population vectors in the early olfactory system of locust (Mazor and Laurent, 2005; Stopfer et al., 2003; Wehr and Laurent, 1996; Laurent, 2002) or zebrafish (Friedrich et al., 2004; Friedrich and Laurent, 2001; Niessing and Friedrich, 2010). Similar phenomena have been described in the leech (Briggman et al., 2005) and the motor cortex of rodents and primates (Churchland et al., 2012; Peters et al., 2014). The turtle neural sequences may thus be the local expression of broader dynamics representing the evolution of activity in networks (Laurent et al., 2001). These patterns would be the expression of stable transient attractors resulting in part from connectivity (Rabinovich et al., 2008; Rabinovich and Varona, 2011) and the expression of basic building blocks of neural systems (Luczak et al., 2015).

Our results underline the relevance of theoretical work on activity propagation in feed-forward networks (Abeles, 1991; Diesmann et al., 1999; Griffith, 1963; Kumar et al., 2010; Reyes, 2003; Vogels et al., 2005). In Abeles's approach, the divergent-convergent structure of neural networks is reframed as generating virtual layers along which information is reliably transferred. Depending on network parameters (sparseness, synaptic weights) and seed activation, activity can propagate synchronously or asynchronously (Kumar et al., 2010). Bienenstock (1995) extended the attributes of such chains to bind elemental features. Izhikevich examined related phenomena that exploit precise conduction delays, generating systems of high memory capacity (Izhikevich, 2006). Finally, important questions arise as to how deterministic sequences arise over time (Fiete et al., 2010; Triplett et al., 2018). If sequences reflect connectivity, they must depend on past experience. Such a link to past history recalls the early work of James (1890) and Hebb's "phase-sequences" (Hebb, 1949). Whether the sequences we describe are a result of past experience, as they are in songbird, should be tested.

STAR★METHODS

Detailed methods are provided in the online version of this paper and include the following:

- KEY RESOURCES TABLE
- LEAD CONTACT AND MATERIALS AVAILABILITY
- EXPERIMENTAL MODEL AND SUBJECT DETAILS
- METHOD DETAILS
  - Surgery and Cortex slab preparation
  - Genetic Transfection
  - Microelectrode Array (MEA) recordings
  - Whole-cell patch-clamp (WCPC) recordings of pyramidal neurons
  - Visually-guided WCPC recordings from multiple pyramidal neurons
  - Optogenetic Stimulation
  - Histology
- QUANTIFICATION AND STATISTICAL ANALYSIS
  - Unit identification as a "follower."
  - Sequence graphs
  - Entropy
  - Rank correlation
  - Synaptic connectivity
  - Follower-spike realignment
  - Follower-AP phase relative to V_m fluctuation of depolarized PN
  - Spatial center of mass calculation
  - Balanced activity
  - Spontaneous sequences
- DATA AND CODE AVAILABILITY

SUPPLEMENTAL INFORMATION

Supplemental Information can be found online at https://doi.org/10.1016/j.neuron.2019.07.017.

ACKNOWLEDGMENTS

We thank M. Klinkmann for help with surgery; A. Arends and A. Macias for technical assistance; and Maria Tosches, Julijana Gjorgjieva, Sam Reiter,

Luis Riquelme, and Hiroshi Ito for suggestions and comments on earlier versions of the manuscript. This work was funded by the Max Planck Society (G.L.), the European Research Council under the EU's 7th framework agreement (FP7/2007-2013)/grant 322705 (G.L.), the Minerva Foundation (M.S.-I.), and the Boehringer Ingelheim Fonds (M.H.).

AUTHOR CONTRIBUTIONS

M.H. and G.L. designed the study. M.H. conducted the combined intra- and extracellular experiments. L.P. and M.S-I. conducted optogenetic experiments. M.H. and M.S-I. analyzed the data. G.L., M.H., and M.S-I. wrote the manuscript.

DECLARATION OF INTERESTS

The authors declare no competing interests.

Received: November 12, 2018
Revised: May 10, 2019
Accepted: July 12, 2019
Published: August 19, 2019

REFERENCES

Abeles, M. (1982). Local Cortical Circuits: An Electrophysiological study (Springer).

Abeles, M. (1991). Corticonics: Neural Circuits of the Cerebral Cortex (Cambridge University Press).

Abeles, M., Bergman, H., Margalit, E., and Vaadia, E. (1993). Spatiotemporal firing patterns in the frontal cortex of behaving monkeys. J. Neurophysiol. *70*, 1629–1638.

Ascoli, G.A., Alonso-Nanclares, L., Anderson, S.A., Barrionuevo, G., Benavides-Piccione, R., Burkhalter, A., Buzsáki, G., Cauli, B., Defelipe, J., Fairén, A., et al.; Petilla Interneuron Nomenclature Group (2008). Petilla terminology: nomenclature of features of GABAergic interneurons of the cerebral cortex. Nat. Rev. Neurosci. *9*, 557–568.

Bazelot, M., Teleńczuk, M.T., and Miles, R. (2016). Single CA3 pyramidal cells trigger sharp waves in vitro by exciting interneurones. J. Physiol. *594*, 2565–2577.

Beggs, J.M., and Plenz, D. (2003). Neuronal avalanches in neocortical circuits. J. Neurosci. *23*, 11167–11177.

Berg, R.W., Alaburda, A., and Hounsgaard, J. (2007). Balanced inhibition and excitation drive spike activity in spinal half-centers. Science *315*, 390–393.

Bienenstock, E. (1995). A model of neocortex. Network *6*, 179–224.

Bonifazi, P., Goldin, M., Picardo, M.A., Jorquera, I., Cattani, A., Bianconi, G., Represa, A., Ben-Ari, Y., and Cossart, R. (2009). GABAergic hub neurons orchestrate synchrony in developing hippocampal networks. Science *326*, 1419–1424.

Brainard, D.H. (1997). The psychophysics toolbox. Spat. Vis. *10*, 433–436.

Brecht, M., Schneider, M., Sakmann, B., and Margrie, T.W. (2004). Whisker movements evoked by stimulation of single pyramidal cells in rat motor cortex. Nature *427*, 704–710.

Briggman, K.L., Abarbanel, H.D., and Kristan, W.B., Jr. (2005). Optical imaging of neuronal populations during decision-making. Science *307*, 896–901.

Churchland, M.M., Cunningham, J.P., Kaufman, M.T., Foster, J.D., Nuyujukian, P., Ryu, S.I., and Shenoy, K.V. (2012). Neural population dynamics during reaching. Nature *487*, 51–56.

Connors, B.W., and Kriegstein, A.R. (1986). Cellular physiology of the turtle visual cortex: distinctive properties of pyramidal and stellate neurons. J. Neurosci. *6*, 164–177.

Couey, J.J., Witoelar, A., Zhang, S.-J., Zheng, K., Ye, J., Dunn, B., Czajkowski, R., Moser, M.-B., Moser, E.I., Roudi, Y., and Witter, M.P. (2013). Recurrent inhibitory circuitry as a mechanism for grid formation. Nat. Neurosci. *16*, 318–324.

Cuntz, H., Forstner, F., Borst, A., and Häusser, M. (2011). The TREES toolbox—probing the basis of axonal and dendritic branching. Neuroinformatics *9*, 91–96.

Diba, K., and Buzsáki, G. (2007). Forward and reverse hippocampal place-cell sequences during ripples. Nat. Neurosci. *10*, 1241–1242.

Diesmann, M., Gewaltig, M.-O., and Aertsen, A. (1999). Stable propagation of synchronous spiking in cortical neural networks. Nature *402*, 529–533.

Dragoi, G., and Tonegawa, S. (2011). Preplay of future place cell sequences by hippocampal cellular assemblies. Nature *469*, 397–401.

Dragoi, G., and Tonegawa, S. (2013). Distinct preplay of multiple novel spatial experiences in the rat. Proc. Natl. Acad. Sci. USA *110*, 9100–9105.

Eckmann, J.-P., Jacobi, S., Marom, S., Moses, E., and Zbinden, C. (2008). Leader neurons in population bursts of 2D living neural networks. New J. Phys. *10*, 015011.

Engel, A.K., Fries, P., and Singer, W. (2001). Dynamic predictions: oscillations and synchrony in top-down processing. Nat. Rev. Neurosci. *2*, 704–716.

Fiete, I.R., Senn, W., Wang, C.Z.H., and Hahnloser, R.H.R. (2010). Spike-time-dependent plasticity and heterosynaptic competition organize networks to produce long scale-free sequences of neural activity. Neuron *65*, 563–576.

Foster, D.J., and Wilson, M.A. (2006). Reverse replay of behavioural sequences in hippocampal place cells during the awake state. Nature *440*, 680–683.

Fournier, J., Müller, C.M., and Laurent, G. (2015). Looking for the roots of cortical sensory computation in three-layered cortices. Curr. Opin. Neurobiol. *31*, 119–126.

Fournier, J., Müller, C.M., Schneider, I., and Laurent, G. (2018). Spatial information in a non-retinotopic visual cortex. Neuron *97*, 164–180.e7.

Friedrich, R.W., and Laurent, G. (2001). Dynamic optimization of odor representations by slow temporal patterning of mitral cell activity. Science *291*, 889–894.

Friedrich, R.W., Habermann, C.J., and Laurent, G. (2004). Multiplexing using synchrony in the zebrafish olfactory bulb. Nat. Neurosci. *7*, 862–871.

Friston, K. (2010). The free-energy principle: a unified brain theory? Nat. Rev. Neurosci. *11*, 127–138.

Friston, K. (2018). Does predictive coding have a future? Nat. Neurosci. *21*, 1019–1021.

Griffith, J.S. (1963). On the stability of brain-like structures. Biophys. J. *3*, 299–308.

Hahnloser, R.H.R., Kozhevnikov, A.A., and Fee, M.S. (2002). An ultra-sparse code underlies the generation of neural sequences in a songbird. Nature *419*, 65–70.

Hebb, D. (1949). The Organization of Behavior: a Neuropsychological Theory (Wiley).

Hemberger, M., Pammer, L., and Laurent, G. (2016). Comparative approaches to cortical microcircuits. Curr. Opin. Neurobiol. *41*, 24–30.

Henze, D.A., Wittner, L., and Buzsáki, G. (2002). Single granule cells reliably discharge targets in the hippocampal CA3 network in vivo. Nat. Neurosci. *5*, 790–795.

Houweling, A.R., and Brecht, M. (2008). Behavioural report of single neuron stimulation in somatosensory cortex. Nature *451*, 65–68.

Isaacson, J.S., and Scanziani, M. (2011). How inhibition shapes cortical activity. Neuron *72*, 231–243.

Izhikevich, E.M. (2006). Polychronization: computation with spikes. Neural Comput. *18*, 245–282.

James, W. (1890). The Principles of Psychology (Henry Holt and Company).

Jarvis, E.D., Güntürkün, O., Bruce, L., Csillag, A., Karten, H., Kuenzel, W., Medina, L., Paxinos, G., Perkel, D.J., Shimizu, T., et al.; Avian Brain

Nomenclature Consortium (2005). Avian brains and a new understanding of vertebrate brain evolution. Nat. Rev. Neurosci. *6*, 151–159.

Klausberger, T., Magill, P.J., Márton, L.F., Roberts, J.D.B., Cobden, P.M., Buzsáki, G., and Somogyi, P. (2003). Brain-state- and cell-type-specific firing of hippocampal interneurons in vivo. Nature *421*, 844–848.

Kriegstein, A.R., and Connors, B.W. (1986). Cellular physiology of the turtle visual cortex: synaptic properties and intrinsic circuitry. J. Neurosci. *6*, 178–191.

Kumar, A., Rotter, S., and Aertsen, A. (2010). Spiking activity propagation in neuronal networks: reconciling different perspectives on neural coding. Nat. Rev. Neurosci. *11*, 615–627.

Laurent, G. (2002). Olfactory network dynamics and the coding of multidimensional signals. Nat. Rev. Neurosci. *3*, 884–895.

Laurent, G., Stopfer, M., Friedrich, R.W., Rabinovich, M.I., Volkovskii, A., and Abarbanel, H.D. (2001). Odor encoding as an active, dynamical process: experiments, computation, and theory. Annu. Rev. Neurosci. *24*, 263–297.

Lefort, S., Tomm, C., Floyd Sarria, J.C., and Petersen, C.C.H. (2009). The excitatory neuronal network of the C2 barrel column in mouse primary somatosensory cortex. Neuron *61*, 301–316.

Li, C.Y.T., Poo, M.M., and Dan, Y. (2009). Burst spiking of a single cortical neuron modifies global brain state. Science *324*, 643–646.

Lonardoni, D., Amin, H., Di Marco, S., Maccione, A., Berdondini, L., and Nieus, T. (2017). Recurrently connected and localized neuronal communities initiate coordinated spontaneous activity in neuronal networks. PLoS Comput. Biol. *13*, e1005672.

London, M., Roth, A., Beeren, L., Häusser, M., and Latham, P.E. (2010). Sensitivity to perturbations in vivo implies high noise and suggests rate coding in cortex. Nature *466*, 123–127.

Long, M.A., and Fee, M.S. (2008). Using temperature to analyse temporal dynamics in the songbird motor pathway. Nature *456*, 189–194.

Long, M.A., Jin, D.Z., and Fee, M.S. (2010). Support for a synaptic chain model of neuronal sequence generation. Nature *468*, 394–399.

Luczak, A., Barthó, P., Marguet, S.L., Buzsáki, G., and Harris, K.D. (2007). Sequential structure of neocortical spontaneous activity in vivo. Proc. Natl. Acad. Sci. USA *104*, 347–352.

Luczak, A., Barthó, P., and Harris, K.D. (2009). Spontaneous events outline the realm of possible sensory responses in neocortical populations. Neuron *62*, 413–425.

Luczak, A., McNaughton, B.L., and Harris, K.D. (2015). Packet-based communication in the cortex. Nat. Rev. Neurosci. *16*, 745–755.

Mazor, O., and Laurent, G. (2005). Transient dynamics versus fixed points in odor representations by locust antennal lobe projection neurons. Neuron *48*, 661–673.

Mazurskaya, P.Z. (1973a). Organization of receptive fields in the forebrain of Emys orbicularis. Neurosci. Behav. Physiol. *6*, 311–318.

Mazurskaya, P.Z. (1973b). Retinal projection in the forebrain of Emys orbicularis. Neurosci. Behav. Physiol. *6*, 75–82.

Molnár, G., Oláh, S., Komlósi, G., Füle, M., Szabadics, J., Varga, C., Barzó, P., and Tamás, G. (2008). Complex events initiated by individual spikes in the human cerebral cortex. PLoS Biol. *6*, e222.

Montiel, J.F., Vasistha, N.A., Garcia-Moreno, F., and Molnár, Z. (2016). From sauropsids to mammals and back: New approaches to comparative cortical development. J. Comp. Neurol. *524*, 630–645.

Nádasdy, Z., Hirase, H., Czurkó, A., Csicsvari, J., and Buzsáki, G. (1999). Replay and time compression of recurring spike sequences in the hippocampus. J. Neurosci. *19*, 9497–9507.

Naumann, R.K., Ondracek, J.M., Reiter, S., Shein-Idelson, M., Tosches, M.A., Yamawaki, T.M., and Laurent, G. (2015). The reptilian brain. Curr. Biol. *25*, R317–R321.

Niessing, J., and Friedrich, R.W. (2010). Olfactory pattern classification by discrete neuronal network states. Nature *465*, 47–52.

Okubo, T.S., Mackevicius, E.L., Payne, H.L., Lynch, G.F., and Fee, M.S. (2015). Growth and splitting of neural sequences in songbird vocal development. Nature *528*, 352–357.

Oram, M.W., Wiener, M.C., Lestienne, R., and Richmond, B.J. (1999). Stochastic nature of precisely timed spike patterns in visual system neuronal responses. J. Neurophysiol. *81*, 3021–3033.

Pammer, L. (2018). Explorations of turtle cortex function through molecular, optogenetic and electrophysiological techniques. PhD thesis (Goethe University Frankfurt).

Peterlin, Z.A., Kozloski, J., Mao, B.Q., Tsiola, A., and Yuste, R. (2000). Optical probing of neuronal circuits with calcium indicators. Proc. Natl. Acad. Sci. USA *97*, 3619–3624.

Peters, A.J., Chen, S.X., and Komiyama, T. (2014). Emergence of reproducible spatiotemporal activity during motor learning. Nature *510*, 263–267.

Pillow, J.W., Shlens, J., Paninski, L., Sher, A., Litke, A.M., Chichilnisky, E.J., and Simoncelli, E.P. (2008). Spatio-temporal correlations and visual signalling in a complete neuronal population. Nature *454*, 995–999.

Prechtl, J.C., Cohen, L.B., Pesaran, B., Mitra, P.P., and Kleinfeld, D. (1997). Visual stimuli induce waves of electrical activity in turtle cortex. Proc. Natl. Acad. Sci. USA *94*, 7621–7626.

Prechtl, J.C., Bullock, T.H., and Kleinfeld, D. (2000). Direct evidence for local oscillatory current sources and intracortical phase gradients in turtle visual cortex. Proc. Natl. Acad. Sci. USA *97*, 877–882.

Prut, Y., Vaadia, E., Bergman, H., Haalman, I., Slovin, H., and Abeles, M. (1998). Spatiotemporal structure of cortical activity: properties and behavioral relevance. J. Neurophysiol. *79*, 2857–2874.

Puelles, L., Sandoval, J.E., del Corral, R., Ferran, J.L., Alonso, A., and Martínez-de-la-Torre, M. (2017). The pallium in reptiles and birds in the light of the updated tetrapartite pallium model. In Evolution of Nervous Systems, J.H. Kaas, ed. (Elsevier), pp. 519–555.

Rabinovich, M.I., and Varona, P. (2011). Robust transient dynamics and brain functions. Front. Comput. Neurosci. *5*, 24.

Rabinovich, M., Huerta, R., and Laurent, G. (2008). Neuroscience. Transient dynamics for neural processing. Science *321*, 48–50.

Reyes, A.D. (2003). Synchrony-dependent propagation of firing rate in iteratively constructed networks in vitro. Nat. Neurosci. *6*, 593–599.

Rupprecht, P., and Friedrich, R.W. (2018). Precise synaptic balance in the zebrafish homolog of olfactory cortex. Neuron *100*, 669–683.e5.

Schneidman, E., Berry, M.J., 2nd, Segev, R., and Bialek, W. (2006). Weak pairwise correlations imply strongly correlated network states in a neural population. Nature *440*, 1007–1012.

Shein-Idelson, M., Pammer, L., Hemberger, M., and Laurent, G. (2017). Large-scale mapping of cortical synaptic projections with extracellular electrode arrays. Nat. Methods *14*, 882–890.

Shew, W.L., Clawson, W.P., Pobst, J., Karimipanah, Y., Wright, N.C., and Wessel, R. (2015). Adaptation to sensory input tunes visual cortex to criticality. Nat. Phys. *11*, 659–663.

Song, S., Sjöström, P.J., Reigl, M., Nelson, S., and Chklovskii, D.B. (2005). Highly nonrandom features of synaptic connectivity in local cortical circuits. PLoS Biol. *3*, e68.

Stopfer, M., Jayaraman, V., and Laurent, G. (2003). Intensity versus identity coding in an olfactory system. Neuron *39*, 991–1004.

Striedter, G.F. (1997). The telencephalon of tetrapods in evolution. Brain Behav. Evol. *49*, 179–194.

Tosches, M.A., Yamawaki, T.M., Naumann, R.K., Jacobi, A.A., Tushev, G., and Laurent, G. (2018). Evolution of pallium, hippocampus, and cortical cell types revealed by single-cell transcriptomics in reptiles. Science *360*, 881–888.

Triplett, M.A., Avitan, L., and Goodhill, G.J. (2018). Emergence of spontaneous assembly activity in developing neural networks without afferent input. PLoS Comput. Biol. *14*, e1006421.

van Vreeswijk, C., and Sompolinsky, H. (1996). Chaos in neuronal networks with balanced excitatory and inhibitory activity. Science *274*, 1724–1726.

Vogels, T.P., Rajan, K., and Abbott, L.F. (2005). Neural network dynamics. Annu. Rev. Neurosci. *28*, 357–376.

Vyleta, N.P., Borges-Merjane, C., and Jonas, P. (2016). Plasticity-dependent, full detonation at hippocampal mossy fiber-CA3 pyramidal neuron synapses. eLife *5*, 3386.

Wehr, M., and Laurent, G. (1996). Odour encoding by temporal sequences of firing in oscillating neural assemblies. Nature *384*, 162–166.

Yizhar, O., Fenno, L.E., Davidson, T.J., Mogri, M., and Deisseroth, K. (2011). Optogenetics in neural systems. Neuron *71*, 9–34.

STAR★METHODS

KEY RESOURCES TABLE

REAGENT or RESOURCE	SOURCE	IDENTIFIER
Bacterial and Virus Strains		
AAV2/1-CamKIIa-hChR2(H134R)-mCherry	Yizhar et al., 2011	Addgene 26975
AAV2/1-CamKIIa-hChR2(H134R)-eYFP	Yizhar et al., 2011	Addgene 26969P
Experimental Models: Organisms/Strains		
Trachemys scripta elegans	NASCO Biology, WI, USA	N/A
Chrysemys picta	NASCO Biology, WI, USA	N/A
Software and Algorithms		
MATLAB	https://www.mathworks.com/	MATLAB
Neurolucida	https://www.mbfbioscience.com/	MBF Bioscience
Spike Sorting	Shein-Idelson et al., 2017	SheinIdelson2017
Other		
EPC 10 USB Quadro	HEKA Instruments Inc.	HEKA.com
MEA2100	Multichannel Systems, MCS	https://www.multichannelsystems.com/
MEA256	Multichannel Systems, MCS	https://www.multichannelsystems.com/
MEA1060	Multichannel Systems, MCS	https://www.multichannelsystems.com/
120MEA100/30iR-ITO	Multichannel Systems, MCS	https://www.multichannelsystems.com/
60HexaMEA40/10iR-ITO	Multichannel Systems, MCS	https://www.multichannelsystems.com/
60MEA100/30iR-ITO	Multichannel Systems, MCS	https://www.multichannelsystems.com/
256MEA100/30iR-ITO	Multichannel Systems, MCS	https://www.multichannelsystems.com/

LEAD CONTACT AND MATERIALS AVAILABILITY

This study did not generate new unique reagents. Further information and requests for resources and reagents should be directed to and will be fulfilled by the Lead Contact, Gilles Laurent (gilles.laurent@brain.mpg.de).

EXPERIMENTAL MODEL AND SUBJECT DETAILS

All experimental procedures were performed in accordance with German animal welfare guidelines [permit #V54-19c 20/15- F126/1005 delivered by the Regierungspraesidium Darmstadt, 64278 Darmstadt, Germany (Fr. Dr. Simon)]. Wild-type turtles (*Trachemys scripta elegans* or *Chrysemys picta*) of either sex, weighing 150 to 400 g, were obtained from an open-air breeding colony (NASCO Biology, WI, USA) and housed in a state-of-the-art animal facility.

METHOD DETAILS

Surgery and Cortex slab preparation

Healthy turtles were anesthetized using Ketamine (23mg/kg, IM) and Dexdomitor (75μg/kg, IM). After loss of the corneal reflex, turtles were decapitated and the heads rapidly transferred into cooled turtle ACSF solution (96.5mM NaCl, 2.6mM KCl, 4mM $CaCl_2$, 2mM $MgCl_2$, 31.5mM $NaHCO_3$, 20mM glucose, pH 7.4) bubbled with carbogen gas (95%-O_2 / 5%-CO_2). The skull was opened to access the dorsal surface of the brain; dura mater and arachnoid were carefully removed.

Cortical slabs were prepared with iridectomy scissors after transverse and parasagittal sections of the cortical sheet. Sections were: (1) transv.: slightly posterior to the anterior pole of the cerebral cortex; (2) transv.: 3-5mm caudal to the first incision; (3) parasag.: along the border between medial and dorsal cortices medially; (4) just medial to the olfactory cortex laterally, slightly before where dorsal cortex merges with the dorsoventricular ridge (DVR). We separated right and left hemisphere and marked the posterior end of each slab with a small incision to keep track of the cardinal axes. For pipette penetration through the turtle cortical pia, we sublimated the pia over a 300-400μm-diameter area using a pulsed UV laser (7,000 pulses; 200 Hz; Ex5 Excimer, GAM Laser Inc., FL, USA). Using oblique electrode paths, we obtained patch-clamp recordings in a zone 50-300 μm peripheral to the borders of this area. The cortical tissue was constantly superfused with oxygenated turtle ACSF at room temperature (about 25°C) at 2-6 ml/min.

Genetic Transfection

Turtles were anesthetized using Ketamine (23mg/kg, IM) and Dexdomitor (75μg/kg, IM) and placed in a stereotactic holder. A craniotomy was performed above dorsal cortex. Dura and arachnoid were gently torn open, and the pia was carefully sectioned using iridectomy scissors. An injection needle (pulled and beveled quartz micropipette) was pushed to 500 μm from the pia, at an angle of 45° oriented caudally, and 300 nL of adeno-associated virus (AAV2/1-CamKIIa-hChR2(H134R)-mCherry, Plasmid Addgene 26975; AAV2/1-CamKIIa-hChR2(H134R)-eYFP, Plasmid Addgene 26969P) (Yizhar et al., 2011) were injected at a rate of 100 nl/min (UMP3, World Precision Instruments, USA). After injection, we waited 10 min before retracting the needle. The craniotomy was closed with a glass coverslip and sealed with dental cement. After 4 weeks the turtle was sacrificed, and the cortical slabs were prepared (see above, *Cortex slab preparation*).

Microelectrode Array (MEA) recordings

After surgery and dissection, the preparation was placed on the multi-microelectrode array (MEA) ventricular side down. We used 60-, 120- or 250-channel extracellular electrophysiological recording systems (MEA1060, MEA2100, MEA256 by Multichannel Systems, MCS), with glass embedded titanium-nitrate electrode arrays of 10 or 30μm electrode diameter and 40 or 100μm electrode spacing (120MEA100/30iR-ITO, 256MEA100/30iR-ITO, 60MEA100/30iR-ITO, 60HexaMEA40/10iR-ITO, MCS). Tissue anchors were used to prevent slab movement and to insure stable contact between electrodes and tissue. Anchors consisted of nylon strings or mesh glued on a 300μm-thick platinum ring (with thickness chosen to match that of cortex). The nylon strings applied gentle pressure on the pial surface of the cortex. Sampling rate for extracellular recordings was 20kHz. MEA data were analyzed *en masse* using a custom-designed data analysis pipeline, with spike sorting and 3D-source triangulation, as previously described (Shein-Idelson et al., 2017). In a typical dataset, we could sort between 60 and 400 MEA units, depending on the duration of the simultaneous patch-clamp recording (15-150 minutes) and on intrinsic activity of the preparation.

Whole-cell patch-clamp (WCPC) recordings of pyramidal neurons

Long-shank patch pipettes (6-8 MOhms) were pulled from borosilicate glass with a Sutter P1000 electrode puller. UV-lasered holes in the pia were located by autofluorescence and used as entry points for patch pipettes. Upon > 10% increase of the initial pipette resistance, positive pressure was released to achieve a GOhm seal (success rate 70%). Pyramidal cells (L2) lie some 400μm below the pia; hence they were patched blindly. For paired blind recordings we first positioned both pipettes close to presumed L2, then patched and broke through simultaneously. Pipettes were filled with internal solution (140mM K-gluconate, 4mM NaCl, 14mM Phosphocreatine, 10mM HEPES, 4mM Mg-ATP, 0.3mM Na-GTP, 4mg/ml Biocytin, 0.015mM Alexa-594 or Alexa 488). Experiments were carried out on an upright Olympus BX61WI microscope with 5x and 40x water-immersion objectives. Cells were held for at least 15 minutes to insure filling with biocytin.

Firing of the patched pyramidal neuron was induced by DC pulse injections (pulse protocol, PP). A "trial" was a 10 s-epoch or sweep, each containing 8 successive current pulses. The pulse duration (P) varied between 20ms and 50ms ($P_{1\text{-}8}$ = {30, 50, 30, 30, 50, 50, 50, 20ms}), to evoke 1 to 3 action potentials each with currents between 100pA and 800pA. The inter-pulse intervals (I) varied between 280ms and 3350ms ($I_{1\text{-}7}$ = {830, 550, 1030, 280, 790, 3350, 300ms}). Unequal intervals were chosen to avoid potential rhythmic entrainment and for wide sampling. Pulse durations and inter-pulse intervals remained unchanged over all experiments. Only injected currents varied between experiments, to produce 1-3 APs per current pulse. Trials were repeated in batches of 16 to 131, with 2 s delay between the end of one trial and the beginning of the next. The first current pulse in a trial occurred at t = 1000ms post trial onset. An experiment thus yielded between 128 and 1048 current pulses per pyramidal neuron. If multiple PPs were tested with each cell, one was chosen that minimized follower adaptation (usually the first protocol). For paired stimulation, we first used two identical versions of the PP in each PN alone and then with a ± 10ms time shift. We also synchronized stimulation protocols with 0 delay, and added a temporal delay (dt = ± 10ms) in a subset of the pulses in one of the PNs (see Figure 6A). This second protocol tested several conditions within a single sweep, reducing long-term adaptation. We obtained identical results in one pair tested with both protocols. In some experiments, we raised spontaneous firing rates using superfusion of carbachol (1-20μM). Sorted MEA units were used to trigger PN membrane potential (in current-clamp) or current (in voltage-clamp, V_{hold} = −70 mV or −45 mV). The significance of averaged spike-triggered membrane currents was evaluated by comparison to a time-shuffled average and thresholding (peak amplitude difference ≥ 3pA).

Visually-guided WCPC recordings from multiple pyramidal neurons

We patched sets of up to eight randomly selected neurons using visually guided patching (n = 381 neurons). For these experiments, the slab was placed ventricle side up in a normal recording chamber (i.e., without MEA). Electrodes were approached sequentially, but Giga-Ohm seals were broken simultaneously to achieve whole-cell configuration at similar times across the recorded set. Visibility was similar to that in typical mammalian brain slice preparations. We tested 930 pairs for synaptic connections. Neurons were located within 6 to 722 μm of each other (126 ± 110 μm inter-somatic-distance, mean ± SD).

Optogenetic Stimulation

For optogenetic stimulation a custom-made system was constructed on an inverted microscope. A digital micro-mirror device (DMD) DLP LightCrafter4500 (Texas Instruments, Texas, USA) producing approximately 150 lumens at 15-W LED power consumption was

attached with appropriate lenses to the light port of an Olympus IX73. A set of MATLAB functions (“psychtoolbox”; (Brainard, 1997)) was used to control the DMD and synchronize data acquisition with light stimulation. This setup allowed us to deliver light with a resolution of 912 × 1140 pixels in the field of view (corresponding to submicron resolution with a 20x objective) with a temporal precision of 17 ms. Actual light delivery was further monitored with microsecond precision using a photodiode, to allow precise temporal alignment of neural activity to light onset and offset. In these experiments, 144 square spots of light (26x26 μm each, 2 s stimulus duration) were projected, one at a time, through the glass material of the MEA and onto the cortical slab. The field of view of the 20x objective was 665x665um and was located within the MEA electrode field. Stimulation spots were illuminated in a pseudo-random sequence, repeated 25 times. Light intensity was adjusted such that around one half of the stimulation spots generated just detectable MEA spiking-activity. After the experiment, MEA units were sorted, classified and selected as described above. To quantify the spread of our stimulation spot due to light scattering by the tissue, we did not measure the actual spread of direct photo-excitation. Rather we measured the reflected light intensity after subtracting the background present during periods of no excitation. This measurement indicated that the excited area (defined as the area with intensity greater than 10% of maximal intensity) was 750 μm^2. Considering a density of 3.2 ± 0.9 ChR2-positive cells/100x100 μm^2, we estimate that each stimulation spot excited 0.24 ± 0.06 pyramidal neuron cell bodies on average. (By convention we denote cell density as density per tangential surface area, due to the non-isotropic distribution of somata along *z* in this cortex. We quantified PN density using a max-intensity projection from high-magnification confocal images taken from 30-90μm of the ventral portion of cortex.) Note also that DMD spot illumination usually failed to activate neurons unless illumination fell on an area containing labeled somata, suggesting that neurons were generally not activated by dendritic or axonal illumination alone in our experimental conditions.

Histology

Several images of the preparation (entire slab surface, MEA electrodes and patch pipette tip) were taken during recordings for later spatial alignment. One image of the pipette tip was taken while the pipette was in recording position, and another after repositioning the pipette above the exact *xy* coordinates of the whole-cell recording. These images were used to (1) determine the position of the patched cell with respect to the MEA electrodes and (2) rescale our post hoc reconstructed cell morphologies, to correct for tissue shrinkage and align them to the triangulated positions of extracellular units (see also (Shein-Idelson et al., 2017)).

At the end of an experiment, the tissue was fixed for 24 hours in 100 mM phosphate buffer (PB) (pH 7.4) with 4% PFA (at 4°C). Patched neurons were stained using biocytin. After extensive rinsing in PB and quenching of endogenous peroxidase, cortical slabs were incubated in 2% Triton X-100 solution for permeabilization and subsequently incubated in 1% Triton X-100 containing avidin-biotinylated horseradish peroxidase (ABC-Elite; Camon, Wiesbaden, Germany). We used 3,3-diaminobenzidine (DAB) as a chromogen for visualizing dendritic and axonal arborization. Slabs were then placed in Mowiol (Carl Roth, Germany) or Dako for further processing.

Biocytin-labeled neurons were reconstructed with the aid of Neurolucida software (MicroBrightField) using a Zeiss Axiophot microscope and a 63x Zeiss objective. Cell bodies, dendrites and axons were identified during the reconstruction. The ependymal surface of the slab was also reconstructed. Resulting reconstructions were read into MATLAB using the TREES toolbox (Cuntz et al., 2011).

QUANTIFICATION AND STATISTICAL ANALYSIS

Unit identification as a “follower.”

After spike sorting, we constructed a 1ms-binned spiking matrix aligned with the intracellular membrane potential recording. “Follower” identification was based on a change in firing rate between baseline (pre-pulse) and the epoch of imposed firing in one patched neuron. Firing rates were measured over two 160ms windows (one ending at current pulse onset: baseline FR or BFR; and one starting at current pulse onset: pulse FR or PFR). In a few experiments where the current pulse lasted for 2 s, the FR-measurement windows were 2 s long, ending and starting at current pulse onset. Firing rates were averaged over pulses ($128 \leq n \leq 1048$ pulses). We subtracted < BFR > from < PFR > to yield the “FR modulation” (see Figure S1F for illustration with one experiment). The mode of the distribution of FR modulations per experiment was centered on ~0 (most MEA units were not affected by 1-3 spikes in the depolarized patched neuron). Our selection threshold was 1 standard deviation over the mean of the FR modulation distribution. The selection threshold needed to be low because follower responses often consisted of no more than a single spike.

Sequence graphs

To quantify the median first-spike time for each follower, we used a pulse-aligned PSTH of 2ms bin size. First-spike time jitter (SD of first-spike time) and spike probability were quantified using that histogram, too. The timing of a follower’s first action potential was measured in a window starting with the first action potential of the patched pyramidal neuron and ending 160ms later. The temporal window within which we considered first-spike times for each follower was widened to 200ms to construct the sequence graph for the entire set of 285 followers.

Entropy

To calculate the reliability of follower firing order across trials, we used an entropy-based measure. For every trial, the n followers were ordered according to the time of their first AP. The entropy of the k^{th} fired AP in the AP sequence was calculated across the identity of followers: $E_k = -\sum P_i \log2(P_i)$, where P_i is the probability of follower i to be the k^{th} to fire. This entropy was divided by the entropy of a uniform distribution — $\sum(1/n)\log2(1/n)$ — resulting in a normalized entropy E_k, a measure between 0 and 1. Zero entropy for the k^{th} AP denotes that the same neuron fired in the k^{th} temporal position in all trials. Since the number of trials was limited and probabilities, P_i, could not be evaluated with full accuracy, we compared the normalized entropy E_k to a shuffled entropy $E_{k,Shuff}$, that was also divided by the entropy of a uniform distribution. For $E_{k,Shuff}$ represented that the same neurons were active in every trial but their ordering was shuffled. The shuffling procedure was repeated over 100 random permutations and the results were averaged. $E_{k,Shuff}$ served as our null hypothesis. If some followers did not fire during a trial (number of neuron in the k^{th} position divided by the number of trials was less than 1), we added to P_i of all neurons an equal amount such that $\sum P_i = 1$. To quantify significant sequential activity across the dataset we calculated for each PN and every AP order (1st, 2nd, ... fired AP following current injection) the 0.05 quantile of the empirical distribution of shuffled entropy values (QE) over 1000 realizations. A given order for a given PN was considered reliable if the calculated entropy for this order was smaller than QE.

Rank correlation

To measure sequence similarity, we calculated average sequence rank correlations and compared them to ones obtained with shuffled data. Specifically, for every current injection k, we calculated the order matrix between neurons i and j, $O_k(i,j)$, with 1 if neuron i fired its first spike before neuron j, -1 if neuron j fired its first spike before neuron i and 0 if they fired within the same 2-ms bin. Next, we calculated the order correlation matrix between the k^{th} and l^{th} current injections, $O_{k,l}(i,j)$, by multiplying these two matrices. To quantify the similarity of ordering between the i^{th} and all other neurons, $S_{k,l}(i)$, we averaged each column of $O_{k,l}(i,j)$ over all other neurons (rows) that were active in both current injection events:

$$S_{k,l}(i) = \frac{1}{N_{active}} \sum_{i \neq j,\ j\ active} O_{k,l}(i,j)$$

$S_{k,l}(i) = 1$ if neuron i showed similar ordering relative to all other neurons across the two current pulses k and l.

$S_{k,l}(i) = -1$ if the relative ordering was reversed.

$S_{k,l}(i) = 0$ if ordering was random on average.

Finally, we averaged over all pairs of current pulses to get the rank correlation for each neuron r(i). Notice that the rank correlation could be calculated between a neuron and all other neurons or between a neuron and its nearest neighbors in time.

To calculate the latter, we first ordered the neurons according to the median (across all trials) delay to their first spike following current injection. We used this order to calculate r(i) not over all neurons but over the nearest neighbors, Rnn(i). This gives a local measure (in time) of the rank correlation along the sequence.

We compared results over 50 realizations in which we kept the same spike times but shuffled them between neurons. This shuffling was always performed only on the population of active neurons within each current injection. For these calculations we used the 1^{st} and 7^{th} pulse in each current injection sweep, but using all pulses gave similar results. Statistics are calculated over all PNs with a minimum of 10 followers (n = 9, Figure S2 J-K).

Synaptic connectivity

Our assignment of excitatory monosynaptic connections was done as in previous studies (e.g., Song et al., 2005 and Lefort et al., 2009). We used short positive current pulses to depolarize one patched neuron across firing threshold (putative pre) while monitoring the membrane potential of other patched neurons (putative post). Membrane potentials of putative postsynaptic neurons were averaged over a minimum of 10 (up to several hundred) repeated pulses, aligned to the pre- action potential time. After averaging, the membrane potential of a putative postsynaptic neuron showed a depolarizing deflection with sharp onset (reflecting low delay jitter) of characteristic asymmetric shape, following the causal action potential with 0.5-4ms delay. EPSPs amplitudes as small as 0.01mV have been reported using this method (Song et al., 2005). Low jitter was confirmed by superimposing individual sweeps. Sometimes an excitatory synaptic connection became apparent only after multiple successive stimuli, suggestive of short-term synaptic facilitation. Facilitating synapses were not very frequent in the dataset (n = 10, 8/10 were E to I). The EPSP amplitude histogram in Figure 3C includes only the synaptic amplitudes elicited by the first presynaptic spike within a train. EPSP amplitudes were measured at a holding potential V_{hold} of -72 mV to -60 mV. We routinely tested for lateral inhibition (221 pairs tested, $V_{hold} = -60$ mV to -50 mV).

A polysynaptic inhibitory pair (E-I-other, where I or more interposed neurons such as E-I were not recorded) was identified if an IPSP in "other" was locked to the action potential of E with a delay > 4ms. We recorded several times from an E neuron that elicited a monosynaptic EPSP (< 3ms delay) in one interneuron and a reliable polysynaptic IPSPs (> 4ms delay) in a simultaneously recorded other E neuron. The latest recorded onset of polysynaptic inhibition between PNs was 137ms. Median and 25^{th} and 75^{th} percentiles of onset of indirect inhibition was 35ms [15, 55]. Polysynaptic connectivity was thus distinguished from direct connections by longer delays, increased PSP-onset jitter, and increased event failure rate.

Follower-spike realignment

To examine the maintenance of precision despite accumulating errors, we examined the dispersion in firing following the realignment of spike sequences to different followers. We chose one follower (seed follower) and time shifted the trials so that the seed follower always fired at t = 0. We then calculated the inter-quartile range (IQR) of the first-spike time (over all sweeps in two chosen pulses, e.g., 1 and 7, of 8 pulses per sweep) for each follower that fired after the seed follower (median firing time across trials > 0) and compared it to the IQR of the same follower before time shifting. We pooled data of the difference in IQR between the shifted and non-shifted trials for all patched PNs with at least 5 followers that fired in more than half of all trials

Follower-AP phase relative to V_m fluctuation of depolarized PN

Phase histograms were constructed from spike-triggered averages of the instantaneous V_m phase. V_m phase was determined from the Hilbert transform of the low-pass filtered V_m (80Hz) after de-trending. We used de-trending to remove very low frequency fluctuations following current injection. This was done by subtracting a cubic smooth spline (csaps function in MATLAB) with a weight defined by A = 10*exp(-t/a)+3 (a = 25ms) from the membrane potential. We analyzed V_m traces starting from a time point defined by the maximal concavity of the low-passed V_m (40Hz). The 40Hz filtered was not used for the phase analysis but only to define the starting point of the analysis (time from maximal concavity). Phase analysis was performed on the 80Hz-filtered signal only. This procedure helped to avoid the sharp decline in V_m right after the current injection.

Spatial center of mass calculation

The pulse-averaged PSTHs and positions of all identified followers were used to calculate the spatial (*x*-*y*) center-of-mass of activity over time for each pulse (Figure 5A-B).

Balanced activity

We compared the response strengths of followers over different time delay conditions (*dt* = 0ms and *dt* = ± 10ms). Responses with *dt* = 0 were compared to the arithmetic sum of responses evoked by each pyramidal neuron alone. Responses with *dt* = 0 were further compared to those with *dt* = ± 10ms. Response strength per condition was quantified for each follower as its mean firing rate of the pulse-aligned PSTH over 300ms, 400ms and 600ms. Follower AP probability was quantified as p of finding one follower spike within 200ms over pulses/trials. Of the seven paired PN recordings in Figure 6 (holding time > 30 min), three were used for detailed analysis (n = 97 followers of 688 (275+276+137) sorted units). Note that the paired activation conditions (*dt = 0 and dt* = ± 10ms) often recruited new followers, not present when activating each pyramidal neuron alone. Followers that responded only during time-shifted protocols are not counted in our n = 285 follower count for the entire dataset. One pair had no detectable followers. In another pair, network activity was too high to apply reliable follower extraction based on our simple metrics. In two further pairs followers adapted too quickly to draw fair comparisons across successive *dt* protocols. Rate changes across 97 followers were not significantly different from a distribution with zero median (p = 0.53, Wilcoxon signed rank test).

Spontaneous sequences

We occasionally observed sequential activity of recorded units in the absence of PN activation by current injection (Figure S2B), but spontaneous events containing many sequentially activated neurons were rare. Pairwise correlations between recorded units were observed consistently but cross-correlation functions had wide peaks. Although only about 1.2% of pairs (n = 932,682 from 29 recordings) reached high correlation values r > 0.3, 13.0% of neurons had at least one such correlated partner.

DATA AND CODE AVAILABILITY

The data and code supporting the current study have not been deposited in a public repository (because of their size), but are available from the corresponding author/Lead contact Gilles Laurent (gilles.laurent@brain.mpg.de) on request.